

HOneY-BeeS

II. Be-X-ray binaries as testbeds for spectroscopic studies of Be stars

S. Janssens^{1,2}, H. Sana^{1,3}, T. Shenar⁴, J. Bodensteiner⁵, and M. Abdul-Masih^{6,7}

¹ Institute of Astronomy, KU Leuven, Celestijnenlaan 200D, 3001 Leuven, Belgium

² Research Center for the Early Universe, Graduate School of Science, University of Tokyo, Bunkyo, Tokyo 113-0033, Japan
e-mail: soetkinjanssens@g.ecc.u-tokyo.ac.jp

³ Leuven Gravity Institute, KU Leuven, Celestijnenlaan 200D, box 2415, 3001 Leuven, Belgium

⁴ Tel Aviv University, The School of Physics and Astronomy, Tel Aviv 6997801, Israel

⁵ Anton Pannekoek Institute for Astronomy, Science Park 904, 1098 XH, Amsterdam, The Netherlands

⁶ Instituto de Astrofísica de Canarias, C. Vía Láctea, s/n, 38205 La Laguna, Santa Cruz de Tenerife, Spain

⁷ Universidad de La Laguna, Departamento de Astrofísica, Av. Astrofísico Francisco Sánchez s/n, 38206 La Laguna, Tenerife, Spain

Received 10 August 2025 / Accepted 10 December 2025

ABSTRACT

Context. The majority of massive classical Be stars – rapidly rotating stars with decretion discs – are suggested to be binary interactions products. Their rapid rotation and often strong, variable, and emission-line dominated spectrum, make spectroscopic analysis challenging. Therefore, robust binary properties and meaningful statistical constraints are currently still lacking for the Be population.

Aims. We aim to use Be-X-ray binaries, and their orbital periods derived from the X-rays, as benchmarks to investigate the reliability of different spectral lines and numerical methods for the measuring of radial-velocities and orbital period determination of Be stars.

Methods. We use multi-epoch high-resolution HERMES spectra of a sample of seven Be-X-ray binaries and compare three different methods to determine radial velocities: cross-correlation, line-profile fitting, and the bisector method, on both absorption and emission lines. We also investigate the effect of different implementations of these methods.

Results. We find that cross-correlation is the most autonomous and convenient method. The bisector method is highly influenced by line-profile variability, while line-profile fitting requires a model template that does not encompass the complexity of Be star line profiles. Cross-correlation can also be implemented on non-Gaussian spectral lines and line blends seen in Be-star spectra. The statistical uncertainties on the radial-velocity precision that is reached by using cross-correlation on the high-resolution HERMES spectra is around 0.2–0.3 km s⁻¹ for H α (emission) and \sim 5 km s⁻¹ for absorption lines, like He I, owing to the lower contrast between the line-depth and the noise level. Potential systematics are not included in the listed values.

Conclusions. We recommend using cross-correlation as the standard method to determine radial velocities for Be stars as it is not dependent on any models and is easily compatible with line blends caused by the rapid rotation of the Be star. In general, whether the goal of a study is to analyse binary statistics of a population or perform an in-depth study of a specific system, we suggest using emission lines since they have a higher precision and less scatter than absorption lines. Here, H β is preferred over H α because of its lesser variability. However, large-scale variability may cause large shifts in emission-line radial velocities, resulting in spurious eccentricities. In this case, orbital solutions should ideally be compared to the lower-signal absorption lines (if present). Finally, we highlight the need for understanding how companion-disc interactions alter the spectroscopic appearance of emission lines.

Key words. Stars: emission-line, Be – binaries:spectroscopic – X-ray: binaries – Techniques: radial velocities

1. Introduction

Classical Be stars are rapidly rotating B-type stars whose spectra show characteristic emission lines attributed to a decretion disc (Struve 1931; Rivinius et al. 2013). About 20% of B stars are of Be spectral type (Porter & Rivinius 2003) and it is suggested that the Be phenomenon originates from single or binary evolution. Several independent studies have recently suggested that the majority of massive Be stars have a binary origin (Boubert & Evans 2018; Bodensteiner et al. 2020b; Hastings et al. 2021; Dallas et al. 2022; Dufton et al. 2022; Dodd et al. 2024; Klement et al. 2024). However, determining the binary statistics of the Be population remains challenging due to their discs, inducing (strong) variability of their emission lines, and to rapid rotation, which broadens their absorption lines significantly. Several optical spectroscopic studies have successfully analysed

Be binaries. Some studies focused on both emission and absorption lines (e.g. Poeckert 1981; Bjorkman et al. 2002; Peters et al. 2008; Nazé et al. 2022; Janssens et al. 2023), while others focused more on emission lines (e.g. Koubský et al. 2012). In some systems, the top and wings of the H α emission line may appear to move in anti-phase (e.g. LB-1; Liu et al. 2019; Abdul-Masih et al. 2020; Shenar et al. 2020) or the H α emission line appears rather stationary while there is actually motion of the star itself (e.g. HR6819; Rivinius et al. 2020; Bodensteiner et al. 2020a). In both cases, black holes (BHs) were falsely assumed to reside in the system, suggesting that (H α) emission lines could be non-optimal to study individual binaries. The complexity and variability of the often double-peaked Be emission lines has different origins. One is the so-called violet-to-red (V/R) variability, where the strength of the blue and red emission peaks cyclically alternates (Okazaki 1991;

Štefl et al. 2009). These variations are often attributed to a spiral density structure in the disc, which could be caused by a companion interacting with the disc (Panoglou et al. 2016, 2018; Rubio et al. 2025). Moreover, variations in the top region of the emission lines from double peaked to triple or single peaked are also observed and mostly affect H α . This variability can be attributed to a companion moving through the outer parts of the disc (e.g. Zamanov et al. 2022). Furthermore, the emission-line strength can cyclically vary over time and can, in some cases, even disappear. This is likely attributed to the formation and depletion of the disc itself (e.g. Doazan et al. 1986; Wisniewski et al. 2010).

So far, the use of photospheric absorption lines is generally preferred over the (variable and complex) emission lines. However, it is not always possible to resort to absorption lines for a spectroscopic analysis as many of them can be contaminated by emission (e.g. several examples in this work and in Koubský et al. 2012; Chojnowski et al. 2018). Moreover, because of their fast rotation, the signal in the broadened absorption lines is often spread and weakened as compared to emission lines, resulting in larger uncertainties and more scatter when determining radial-velocities (RVs). Finally, pulsational variability is also a major source of error for determining RVs of Be stars (e.g. Baade 1987; Baade & Balona 1994). With the aforementioned challenges in mind, the spectroscopic analysis of Be stars could benefit from a standardised methodology to determine reliable RVs.

Be-X-ray binaries (BeXRBs) are a subclass of the high-mass X-ray binaries (HMXBs), where the luminous companion is a Be star. Several of these BeXRBs show regular X-ray outbursts, which are often attributed to the passing of the compact companion through the dense disc. Hence, in many cases, orbital periods can be determined from the X-rays (e.g. Bongiorno et al. 2011; Usui et al. 2012; Ferrigno et al. 2013; Moritani et al. 2018).

This paper is part of the Hermes Observational survey of OeBe Stars (Honey-BeeS). The Honey-BeeS is a multi-epoch spectroscopic program, in which over 200 bright ($V < 12$ mag) northern Be stars are observed (see Bodensteiner, J. et al. in prep. for more details). The stars in Honey-BeeS are classical Be stars with spectral types earlier than B1.5 based on the BeSS database¹. Given the spectral-type cut, the Be stars and their companions are both expected to be massive stars – and thus compact-object progenitors –, such that we focus on double compact-object binary progenitors (see Bodensteiner et al. 2020b).

In this paper, we focus on the BeXRBs in HOney-BeeS. We aim to compare RVs obtained with different methods and different diagnostic lines (absorption and emission) to the orbital information that is found from the X-ray data. This way, we can investigate which methods and diagnostic lines are more reliable and provide the most precise results.

In Sect. 2, we describe the selection of the sample and the newly obtained spectroscopic data. The different methods to measure the RVs are explained in Sect. 3 including an overview of the mechanisms that are expected to give rise to RV variations. The short-term stability of different spectral lines and methods is reported in Sect. 4. We compare different spectral lines and obtain orbital information on targets in Sect. 5. We discuss our results in Sect. 6 and our conclusions in Sect. 7.

¹ <http://basebe.obspm.fr/basebe/>

2. Sample selection and observations

2.1. Sample selection

We searched for BeXRBs in HOney-BeeS through a cross-match with the X-ray catalogues of Liu et al. (2000), Reig (2011), Walter et al. (2015), and Fortin et al. (2023). The cross-match resulted in eight matches, of which five were included in this study: HD 259440, V420 Aur, V615 Cas, V725 Tau, and V831 Cas. Both MWC 656 (Janssens et al. 2023) and BD+47 3129 (Nazé et al. 2022) have already been analysed by means of different methods and spectral lines and were excluded. The system 2E 1752 was not yet analysed in this work due to a lack of data. We included two additional targets that were not listed in BeSS at the time of making the HOney-BeeS catalogue: EM* VES 826 and X Per. In total, we thus have seven BeXRB targets, for which a short description and spectral overview is given in appendix A. The targets and their basic information are listed in Table 1.

2.2. Observations

We used the High-Efficiency and high-Resolution Mercator Echelle Spectrograph (HERMES), mounted on the 1.2m Mercator telescope at the Roque de los Muchachos observatory in La Palma, Spain (Raskin et al. 2011). The data were collected with the high-resolution mode, delivering a spectral resolving power of $R = \lambda/\Delta\lambda \simeq 85000$ and covering the wavelength range 3800–9000 Å with a step size of ~ 0.02 – 0.05 Å. Most of the observations were randomly spread between 2020 and 2024, within the frame of the HOney-BeeS program (see Bodensteiner, J. et al. in prep.). Additionally, all archival HERMES spectra past a two-year proprietary period were also used in this work.

Raw spectra were reduced with the HERMES reduction pipeline (HERMES-DRS, V 7.0), which includes bias correction, flat-fielding, wavelength calibration, cosmic and dark removal, and correction for barycentric motion. All data were normalised with a spline interpolation using the Python package SciPy (Virtanen et al. 2020). The typical signal-to-noise (S/N) per pixel at ~ 4500 Å, and number of spectra N_{spec} are listed in Table 1. The time baseline of the observations is also given in Appendix A.

3. Methods for radial velocity measurements

We used three methods to obtain RVs: cross-correlation (CC, Sect. 3.1), the bisector method (labeled ‘bisec’ in figures, Sect. 3.2), and line-profile fitting (lpf, Sect. 3.3). In Sect. 3.4, we discuss intrinsic variabilities that can affect the RV measurements.

3.1. Cross correlation

By cross-correlating an observational template or a model spectrum with the individual spectra, a CC function is obtained. By fitting a parabola or Gaussian to the maximum region of the CC function, RVs are determined (Zucker 2003). Statistical errors are calculated as described in Zucker (2003).

In this work, CC was done iteratively. In the first iteration, the first spectrum was used as a template. In further iterations, the used template was an average spectrum according to the RVs obtained in the previous iteration. The higher S/N in the templates of later iterations typically lowers the RV uncertainties, especially for weaker lines. The procedure stopped when the RVs of the last three iterations were in agreement within 0.01 km s $^{-1}$.

The derived RVs are not absolute but relative to the master template. Thus, no systemic velocity can be determined. For the goal

Table 1: Target names, spectral type, X-ray orbital period P_X , eccentricity e , spin period P_{spin} , V-band magnitude, S/N around 4500Å, and number of available spectra N_{spec} .

Target id	spectral type	P_X [d]	e	P_{spin} [s]	V mag	S/N at 4500Å	N_{spec}
EM* VES 826	B0.2 Ve	150-155	?	205	10.73	20	9
HD 259440	B0pe	~ 317	?	?	9.12	70	38
V420 Aur	B0 IVpe	?	?	?	7.48	35/70 ^a	187
V615 Cas	B0 Ve	26.5	?	0.269	10.75	35/50 ^b	47
V725 Tau	O9.5 IIIe	110	0.47	104	9.39	70	29
V831 Cas	B1 IIIe	?	?	1400	11.37	30	15
X Per	B0/1 Ve	250	0.11	837	6.72	120	20

Notes See Appendix A for references on periods. ^a The first 142 spectra have S/N ~ 35 , while the others have S/N ~ 70 . ^b The first 18 spectra have S/N ~ 35 , while the others have S/N ~ 70 . ^c Unknown. ^d Multiple values reported in literature.

of this work, which is determining if orbital motion can be detected in BeXRBs, this poses no problem.

3.2. Bisector

To obtain the bisector of a given spectral line, the line is first divided into bins of identical flux ranges in the red and blue wing. In each blue and red flux bin, intermediate RVs are calculated by averaging the RVs of each wavelength point in the bin with respect to the rest wavelength of the spectral line, which were taken from the National Institute of Standards and Technology (NIST) spectral line database². The intermediate RVs of two identical flux bins in the red and blue wing are then averaged to obtain the mean RV (\bar{RV}) of a given flux bin. The \bar{RV} s trace the bisector of the spectral line. The final RV of a spectral line is then obtained by averaging all \bar{RV} s and its uncertainty is determined by the standard deviation of the \bar{RV} s. The derived uncertainty on the RV of the spectral line thus depends on how symmetric the line shape is and will be, in general, very small. The bisector is sensitive to asymmetries in the line and line-profile changes can easily be traced through the bisector. Therefore, it is often used to trace variability in the line profile, but it has already been used to determine RVs (e.g. Gies et al. 1994). We investigate the effect of excluding different bottom and top regions of the lines on the RV determination in Appendix B.

3.3. Line-profile fitting

We fitted Gaussian or Voigt profiles to the spectral lines, with respect to the NIST rest wavelength, by using the python package lmfit (Newville et al. 2014). We used several fit setups: (i) the full spectral line with a single emission or absorption profile, (ii) part of the line while excluding the (variable) top region of an emission line, or (iii) a combination of an emission and absorption profile, which is only fitted for double-peaked emission lines. A cut-off top fit and an emission + absorption fit are marked with ‘cut’ and ‘double’, respectively, in figures.

For double fits, the central wavelengths of the emission and absorption profile were set to be identical, such that they share the same RV. Should we not enforce this, V/R variations in the emission profiles will lead to fits displaying non-equal central wavelengths for the fitted profiles and apparent anti-phase motions.

3.4. Uncertainties and intrinsic variability

One of our goals is to investigate how line variability affects the accuracy of RV measurements obtained from various methods. Informed by these results, we aim to identify variability criteria that would separate intrinsic line-profile variations (e.g. due to discs) from those induced by a companion in a binary system. In this context, we adapt the formalism of Dsilva et al. (2020) for Wolf-Rayet star RV measurements. We consider four main sources of variability in our RV measurements: measurement uncertainties, disc variability, binarity, and pulsations, such that

$$RV_{\text{meas}} = RV_{\text{true}} + \theta_{\text{meas}} + \theta_{\text{disc}} + \theta_{\text{bin}} + \theta_{\text{puls}}, \quad (1)$$

where RV_{meas} is the measured RV and RV_{true} is the true velocity of the star. The θ_{meas} , θ_{disc} , θ_{bin} , and θ_{puls} are (potential) contributions of the measurement process, disc, orbital motion, and pulsations to the measured RV, respectively.

We can take advantage of the fact that these four quantities have a different statistical behavior: 1) θ_{meas} is expected to be mostly affected by random noise, likely Gaussian distributed, and impacted by quantities such as the S/N and the line width. 2) θ_{disc} will mostly impact emission lines, resulting from asymmetries in the disc arising on timescales of days to decades (e.g. Labadie-Bartz et al. 2018). These variabilities can be intrinsic or induced by a companion passing through the disc. Both might shift the RV measurements compared to the RV of the centre-of-mass of the star. 3) θ_{bin} is the orbital motion contribution of the Be star in a binary and will vary periodically over time following Kepler’s law. Timescales for orbital periods are expected to be of the order of months to years if Be stars are post-interaction products (e.g. Hastings et al. 2021; Schürmann et al. 2025). 4) θ_{puls} represents pulsationally induced RV variability, which might be more prominent for the absorption lines. This variability can have time spans of hours to days, and is quite diverse for Be stars (e.g. Porter & Rivinius 2003).

Under the assumption that these quantities are uncorrelated, we can express the variance of our RV sample as

$$\sigma_{\text{tot}}^2 = \sigma_{\text{meas}}^2 + \sigma_{\text{disc}}^2 + \sigma_{\text{bin}}^2 + \sigma_{\text{puls}}^2. \quad (2)$$

On time scales of hours, the ideal case gives us $\sigma_{\text{tot}}^2 \approx \sigma_{\text{meas}}^2$. However, this may be different than the statistical error obtained from the method itself due to, for example, normalisation artifacts or pulsations (σ_{puls}). Nevertheless, this suggests that we can use short cadence RV measurement time series to evaluate σ_{meas} and long timebase series of a single star to place constraints on σ_{disc} . Moreover, emission lines and absorption lines might not have an equal response to pulsational or disc variability. We discuss these aspects further in Sect. 4.

² https://pml.nist.gov/PhysRefData/ASD/levels_form.html

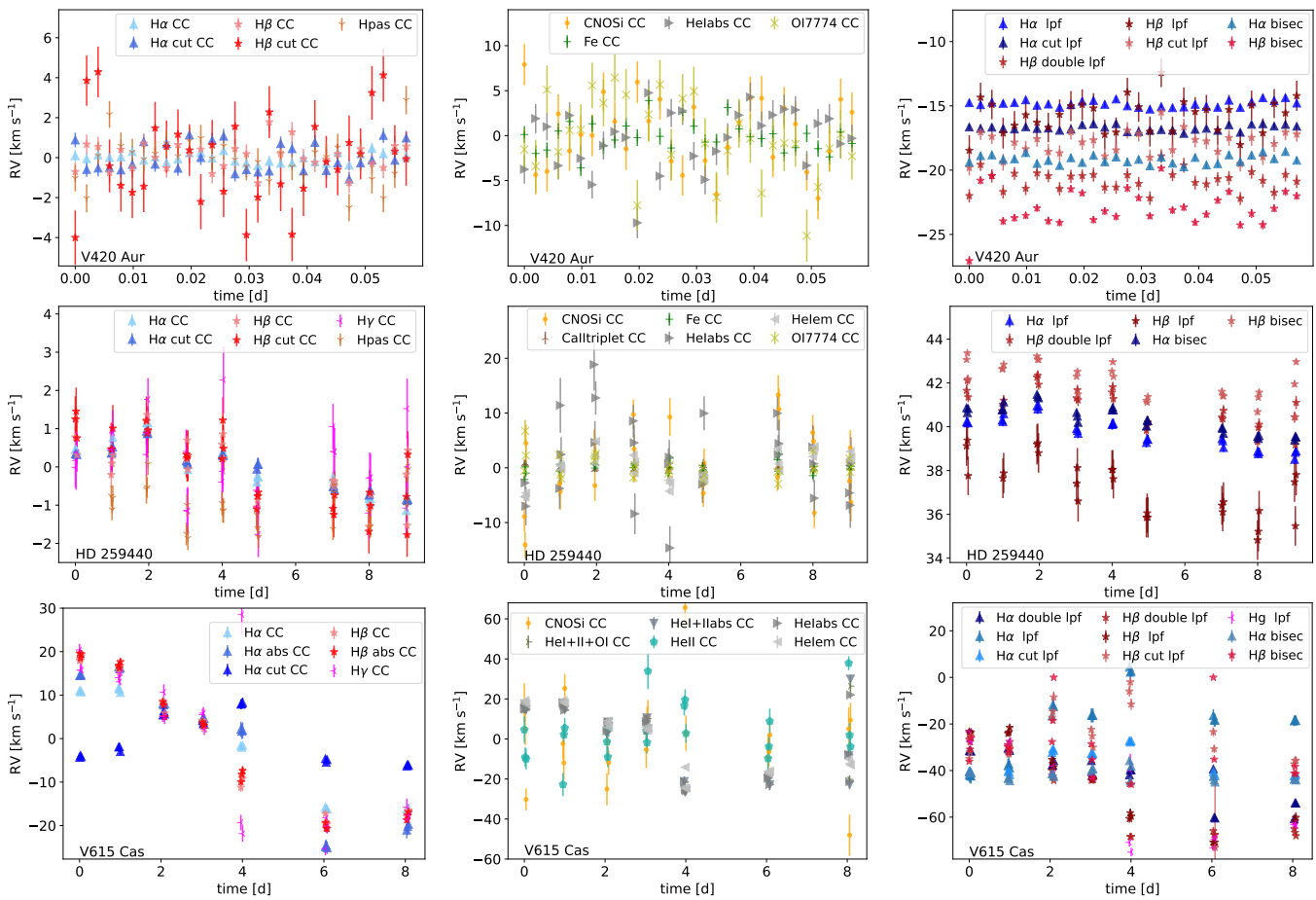


Fig. 1: Radial velocities obtained with different methods on different spectral lines for V420 Aur (top row) for one night, HD 259440 (middle row) for all nights with three consecutive spectra, and V615 Cas (bottom row) for all nights with three consecutive spectra. The x-axis shows the time spectra were taken since the first spectra shown. Left: hydrogen lines and CC. Middle: non-hydrogen lines and CC. Right: hydrogen lines and lpf and bisector. In the legend, ‘Fe’ refers to the Fe II emission lines in the region of 5200Å.

In reality σ_{disc} and σ_{bin} may not be fully uncorrelated, for example when the companion periodically passes through the disc, which is the case for some BeXRBs. Therefore, when measuring RVs from Be stars, a by-eye assessment of the variability in the spectra is necessary to evaluate if the measured RV changes can be true RV measurements for the star or whether they are inferred from disc variability.

4. Benchmarking methods and diagnostic lines

In this section, we determine the stability of different spectral lines and methods on short timescales, providing us with an estimate of σ_{meas} . Indeed, on short time scales of \sim hours, we expect no large RV variations, as suggested in Sect. 3.4 (except for potential pulsations). For this purpose, we used targets for which high-cadence monitoring over a few hours time span is available, which are V420 Aur, HD 259440, and V615 Cas.

We assess which method and spectral line yield a better precision by calculating the root-mean-squared (rms), which is an estimator of the standard deviation using (Bevington & Robinson 2003):

where x_i is the i -th RV measurement with uncertainty σ_i , \bar{x} is the average RV measurement over the considered time span, and N is the number of RV data points. We describe the used lines and methods in Sect. 4.1 and discuss the results in Sect. 4.2.

4.1. Used methods and diagnostic lines

For V420 Aur, we used the CC method on H α , H β , the H Paschen series, the Fe I emission lines in the region of 5150–5380 \AA (listed as ‘Fe’), the He I lines that are in absorption (those marked by a single ‘a’ in Table A1, further referred to as ‘He I abs’), the O I $\lambda\lambda$ 7772,74,75 emission line complex (listed as ‘OI7774’), and the N II, Si IV, N III, O II, and C III lines between 4630–4655 \AA , which are blended due to the rapid rotation of the Be star. We refer to this line blend as the CNOSi line blend. For the bisector and lpf methods, only H α and H β were used.

For HD 259440, we used the same set of lines as for V420 Aur. Additionally, we also measured RVs for Hy, the He I emission lines (those marked with ‘e’ or ‘dp’ in Table A1, further referred to as ‘He I em’), and the Ca II $\lambda\lambda$ 8498, 8542, 8662 (further referred to as ‘Ca I triplet’). For the Ca I triplet, the separation from the H Paschen series is challenging and hence the fit is mostly focused on the blue wing of the Ca emission.

For V615 Cas, we used the CC method on $H\alpha$, $H\beta$, $H\gamma$, He I abs, He I em, the He II lines (in absorption), a combination of He I abs and He II with and without O I 7774, and the CNOSi blend. We

$$\text{rms} = \frac{N}{N-1} \sqrt{\sum_i \frac{(x_i - \bar{x})^2}{\sigma_i^2}} / \sum_i \frac{1}{\sigma_i^2}, \quad (3)$$

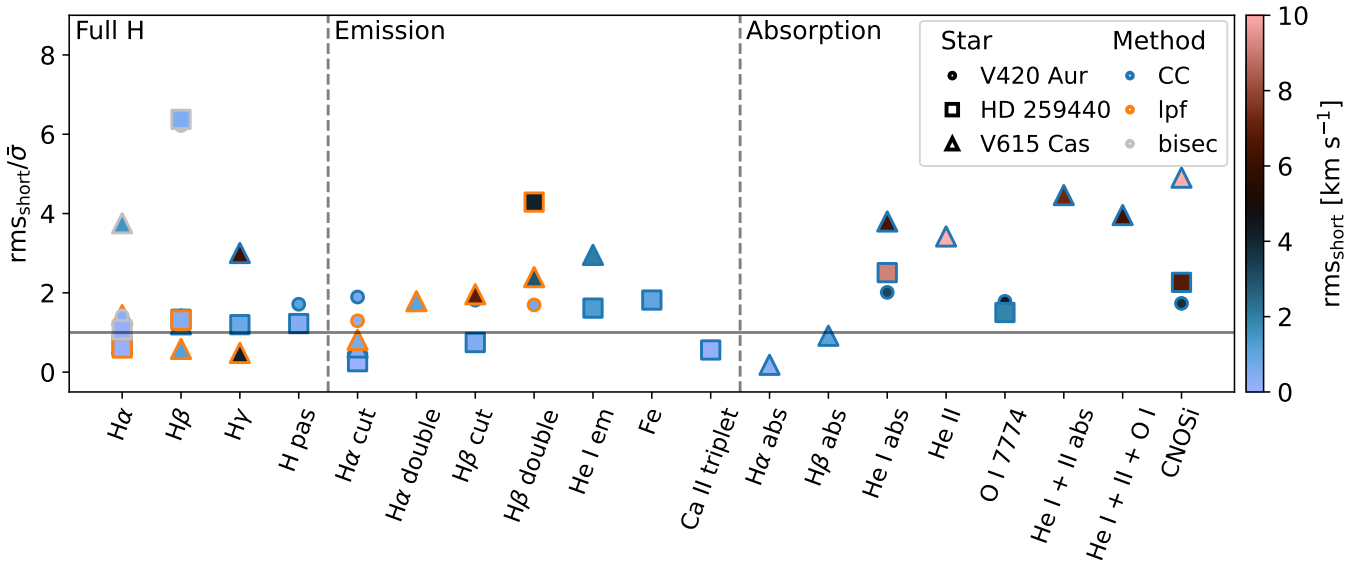


Fig. 2: Ratio of $\text{rms}_{\text{short}}$ and $\bar{\sigma}$ for different spectral lines (indicated on the x-axis) for V420 Aur (circles), HD 259440 (squares), and V615 Cas (triangles). Different methods are indicated with different edge colors. The color map in the symbols indicates the value of $\text{rms}_{\text{short}}$. A value of 1 for $\text{rms}_{\text{short}}/\bar{\sigma}$ is shown with a solid line.

focused the $\text{H}\alpha$ fit on the full line, the emission wings ('cut'), and the absorption component ('abs'). For the lpf and bisector method, we used $\text{H}\alpha$ and $\text{H}\beta$. We also fitted $\text{H}\gamma$ using lpf with an absorption profile. For the single-Gaussian fitted $\text{H}\beta$ (' $\text{H}\beta$ lpf'), the fit focused on the absorption core and not on the emission.

4.2. The stability of the methods and diagnostic lines

The measured RVs for V420 Aur are shown in the top panels of Fig. 1 for the 30 consecutive spectra obtained within a time span of 2h30min in the night of October 12, 2016. The RVs of HD 259440 and V615 Cas are displayed in the middle and bottom rows of Fig. 1, respectively, showing the nights for which three consecutive spectra are available (November 2009). The ratio of the average measurement uncertainties ($\bar{\sigma}$) and rms values for the consecutive spectra ($\text{rms}_{\text{short}}$) are shown in Fig. 2 and individual values are given in Table C1 for the three systems. The rms short is larger than $\bar{\sigma}$ for almost all spectral lines except for $\text{H}\alpha$, which indicates that the measurement uncertainties σ_{meas} obtained from the methods are underestimated. Hence, a smaller precision can be reached on the orbital analysis than what is given by the σ_{meas} . For example, σ_{meas} for $\text{H}\beta$ with CC are underestimated by a factor 1.4-2, even increasing to a factor > 5 when using the bisector method. This extreme increase in the underestimation of σ_{meas} with the bisector method is because the method is much more sensitive to line-profile variability and the method's intrinsic σ_{meas} are very small by construction.

The rms short of absorption lines is larger than for emission lines. For example, typical precisions reached using CC on $\text{H}\alpha$ are $0.2\text{--}0.3 \text{ km s}^{-1}$, as compared to $\sim 5 \text{ km s}^{-1}$ for absorption lines. Generally, the contrast between the intensity of the absorption lines and the noise level is lower than for the emission lines, which could increase the scatter. However, this should already be accounted for in σ_{m} . Instead, there is a high possibility that the rms short increases because pulsational variability at the stellar surface is impacting more effectively the (photospheric) absorption lines than the (disc-dominated) emission lines.

From Figs. 1 and 2, it is clear that stronger (emission) lines, like $\text{H}\alpha$ and $\text{H}\beta$, generally show less scatter than weaker (absorption)

lines, such as He I abs , O I 7774 , or the CNOSi blend. Based on this diagnostic, absorption lines should not necessarily be preferred over emission lines.

However, in the example of V615 Cas, $\text{H}\alpha$ shows significant differences compared to other lines. Depending on which part of the line is used (full line ' $\text{H}\alpha$ ', wings only ' $\text{H}\alpha$ cut', or absorption part only ' $\text{H}\alpha$ abs'), the derived RVs differ significantly. While the $\text{H}\alpha$ absorption component follows the same trend as He I lines and $\text{H}\beta$, the emission parts and the combined fit do not. This is most likely not seen in $\text{H}\beta$ because its emission component is rather weak and the absorption feature dominates. The same is seen for the ' $\text{H}\alpha$ lpf' and ' $\text{H}\alpha$ bisec' as both are tracing the emission-line RV.

For lpf, fitting double-Gaussian profiles is often challenging as good initial guesses need to be provided. Otherwise, the fit can have trouble finding the correct absorption or emission feature if they are rather weak. Using a single Gaussian or Voigt profile often reduces the impact of the initial guesses. However, the fitting becomes less accurate for emission lines with strong absorption cores as the method tries to find a compromise between the emission and the absorption. In this case, cutting out the absorption feature from the single-Gaussian fit improves the fit quality.

To conclude, overall, the precision with which RVs can be determined is of the order of a few km s^{-1} , even when using the weaker absorption lines. While all three methods can yield satisfactory results, CC and bisector are more autonomous than lpf, which often needs tweaking of initial guesses. However, the measurement uncertainties are largely underestimated with the bisector method. Moreover, CC can also be fitted on line blends (e.g. CNOSi) and can easily account for asymmetric line shapes, which is difficult with the bisector.

However, CC does not yield a systemic velocity. This is not a problem for science goals that are looking at relative variability only, but might be a limitation for other goals. Performing CC with a theoretical template may alleviate this issue.

The often weak signal in the absorption lines combined with

Table 2: Orbital solutions for V615 Cas using different spectral lines.

spectral line	P [d]	e	ω [°]	T0	K_1 [km s ⁻¹]	z_0 [km s ⁻¹]	rms
H β	26.506 ± 0.003	0.58 ± 0.13	88 ± 21	10494.39 ± 0.68	14.1 ± 2.6	-23.4 ± 1.6	7.5
H α abs	26.509 ± 0.003	0.53 ± 0.10	61 ± 14	10493.89 ± 0.72	22.8 ± 2.7	-28.0 ± 1.9	11
H α em	26.508 ± 0.008	0.69 ± 0.18	265 ± 18	10499.8 ± 1.1	20.5 ± 6.7	14.9 ± 1.8	7.2
H γ	26.509 ± 0.003	0.70 ± 0.11	109 ± 14	10495.41 ± 0.64	21.3 ± 3.3	-23.3 ± 2.2	11
He 1 abs	26.489 ± 0.009	0.00 ± 0.15	90	10506.02 ± 0.82	19.8 ± 3.1	-27.9 ± 2.5	11
H β	31.055 ± 0.005	0.30 ± 0.12	62 ± 27	10356.9 ± 1.9	15.3 ± 2.3	-26.4 ± 1.6	6.8
H α	31.055 ± 0.007	0.29 ± 0.11	81 ± 30	10358.2 ± 2.2	25.2 ± 4.3	-30.8 ± 2.8	10
He 1 abs	26.093 ± 0.003	0.57 ± 0.08	348 ± 13	10329.46 ± 0.55	21.4 ± 2.4	-29.6 ± 1.8	9.9

Notes Listed uncertainties correspond to 1σ . The last three rows are solutions when using the periods found in the periodograms as initial guesses.

the pulsational variability can result in a large scatter on the RVs and hence less accuracy. Based on the precision that is reached, emission-line RVs can be a good alternative. However, H α -based RVs should be considered with caution as already shown in two BH imposters (LB-1 and HR6819; Liu et al. 2019; Abdul-Masih et al. 2020; Bodensteiner et al. 2020a; Rivinius et al. 2020). While H α is the strongest line in the optical spectrum, it is also the most variable and can lead to RVs that are not following the orbital motion (see also Sect. 5). We suggest that H β , and most likely higher-order Balmer lines, can be a good alternative to absorption lines for RV measurements in the spectra of Be stars. We will further test the reliability of individual spectral lines in Sect. 5, where we search for orbital solutions for the BeXRBs.

5. Searching for periodicities and orbital solutions

In this section, we will present the RV measurements of the targets, together with an orbital fit (if there is sufficient data). We only present results using CC and compare different spectral lines. For V420 Aur, HD 259440, and V615 Cas, we merged the consecutive spectra, taken on timescales of a few hours, to increase the S/N of the spectra for these nights.

Orbital fitting was performed using spinOS³ (Fabry et al. 2021), which uses a non-linear least-squares minimisation. The fitted parameters are orbital period P , eccentricity e , argument of periastron ω ⁴, time of periastron passage T0 (given in BJD – 2 450 000), semi-amplitude of the RV curve K_1 , and the systemic velocity. Since the RVs are measured using CC, this systemic velocity has no physical meaning and is referred to as the zero-point offset z_0 .

For all targets, we also calculated periodograms (for details, see Appendix D). For none of the targets is the X-ray orbital period the most significant period. This already highlights the difficulty of obtaining independent orbital periods and solutions.

We divide our sample into three groups, based on the variability of the emission lines and the prominence of the absorption lines (see Appendix A for an overview of the spectral appearance of the targets). First, we have stars with strong absorption lines and clearly double-peaked emission lines without large-scale variability in our time-series spectra ('group A', Sect. 5.1), in which we only put V615 Cas. Second, we have stars where emission lines are also stable, as for group A, but the signal in

absorption lines is rather weak as they are very broadened, and emission lines are not necessarily double peaked ('group S', Sect. 5.2). Here, we find EM* VES 826 and HD 259440. Third are objects which show large-scale variability in their emission lines ('group LV', Sect. 5.3), which contains V725 Tau, V831 Cas, and X Per.

Lastly, we did not yet classify V420 Aur. For years, V420 Aur shows rather stable absorption lines. Only in a few recent spectra is there notion of V/R variability as well as an apparent increase in emission-line strength. Therefore, we consider V420 Aur to be of group LV, but discuss it separately.

5.1. Group A: strong absorption lines

In this group showing prominent absorption lines, we have one system: V615 Cas, with a reported orbital period of ~ 26.5 d (e.g. Hutchings & Crampton 1981; Taylor & Gregory 1982; D'Aì et al. 2016; López-Miralles et al. 2023). The absorption component in the emission line of H α (see Fig. A4) is strong enough such that RVs of the absorption and emission component can be measured separately.

The data for V615 Cas are spread over 15 years, and, at multiple times, cover large parts of the orbit within one orbital cycle of the reported 26.5 d period. Phase-folded RVs are shown in Fig. 3 for different spectral lines. Orbital solutions are listed in Table 2, where the final column shows the rms values. The orbital solutions with the lowest rms is H β .

The orbital periods and eccentricities mostly agree within 1σ , except for He 1 abs, for which a slightly lower orbital period is found with a zero eccentricity. When fixing P , T0, and e to those found for H β , the rms and reduced χ^2 value have slightly increased compared to the values when not fixing P , T0, and e . However, the RVs of He 1 abs do follow the same trend as those of other spectral lines (left panel of Fig. 3). The origin of the preferred zero eccentricity is unknown.

The last three rows in Table 2 list orbital solution obtained for the highest-amplitude periods in the periodograms (Fig. D1, second row, left panel) of H β and H α ($P = 31.055$ d), and He 1 abs ($P = 26.10$ d) as the initial guess. The rms values have even improved compared to the orbital solutions found when using the X-ray orbital period. This highlights that, even though V615 Cas has the best orbital coverage of all BeXRBs in this study, finding the true orbital period without any beforehand knowledge remains very challenging. The 31 d period could be a beat period due to a precessing disc.

Furthermore, there seems to be an anti-phase motion and an additional 5 d shift in T0 (left panel of Fig. 3) of the RVs from the H α emission wings ('H α em') with respect to other spectral

³ <https://github.com/matthiasfabry/spinOS>

⁴ spinOS fits ω with respect to the companion. Here we list ω with respect to the Be star (i.e. a 180° shift from the returned spinOS value).

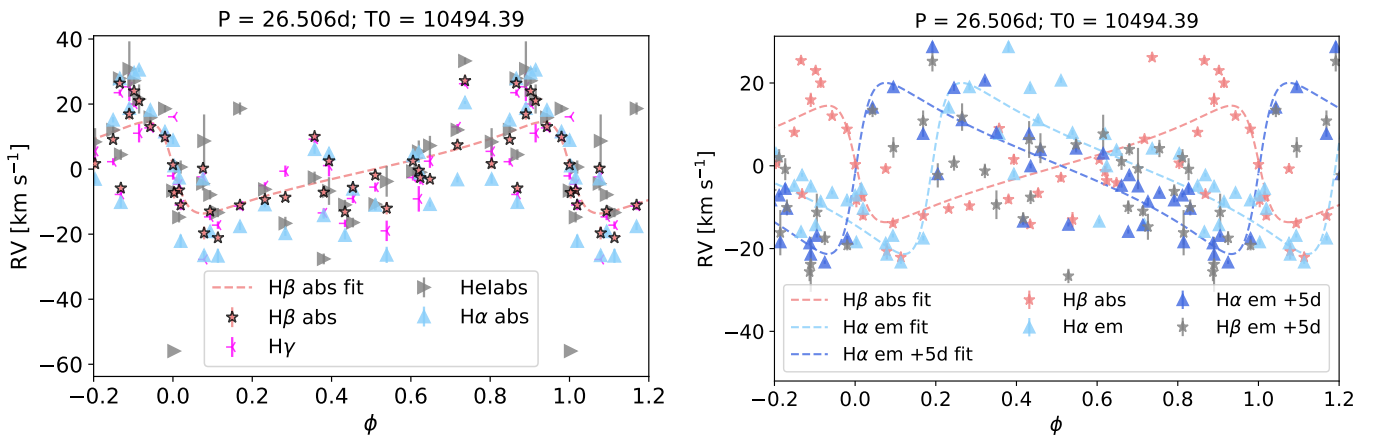


Fig. 3: Phase-folded RVs and fits of V615 Cas with an orbital period of 26.506 d and $T_0 = 10494.39$. Left panel: different spectral lines, excluding $H\alpha$ emission, and the derived $H\beta$ RV curve. Right panel: $H\beta$ and the $H\alpha$ emission component with both RV curves. Darker-blue triangles show $H\alpha$ with a 5 d difference in T_0 (as listed in Table 2). Grey stars show the RVs obtained from $H\beta$ emission, also with a 5 d shift in T_0 .

lines. If this anti-phase orbital motion is true, and not an effect of the moving absorption component, like in LB-1 (Abdul-Masih et al. 2020), it could be attributed to the NS companion, meaning the Be-star mass would be extremely low. More likely, this is a counteracting effect on the disc. Despite the large scatter, $H\beta$ em (grey stars in middle panel of Fig. 3) might follow the same trend as $H\alpha$ em. However, the $H\beta$ emission component is too weak to obtain robust RVs and to fully test this hypothesis.

Based on just one example in group A, both emission and absorption lines trace the orbital period. However, as highlighted above, effectively identifying the orbital motion without prior knowledge is challenging even in this well-observed system. Whether V615 Cas is a special case in group A in terms of anti-phase motion of emission and absorption lines or whether this will be true for most systems in this category remains to be investigated with more targets.

5.2. Group S: stable emission lines with weaker absorption

While the top part of the emission lines of group S systems is slightly variable, the variability is not large enough to affect the general line profile. In contrast to group A, the absorption-line signal of group S systems is rather weak. This results in a large scatter on the absorption-line RVs or the possibility that CC does not even converge (as for EM* VES 826).

The suggested 155 d orbital period for EM* VES 826 is indicated by vertical dashed lines in Fig. 4. The RVs of HD 259440 are shown in Fig. 5, phase-folded onto the 317.3 d orbital period (Adams et al. 2021). While the orbital coverage is currently not optimal, the emission lines seem to trace the orbital period in both cases. However, more data is needed to independently determine orbital periods. Indeed, the data for EM* VES 826 are too sparse to perform orbital fitting and for HD 259440, the periastron passage is only observed during one orbital period.

Nevertheless, for HD 259440 we performed orbital fitting a fixed orbital period of 317.3 d (the X-ray orbital period). Fits for different spectral lines are listed in Table 3 and shown in Fig. 5. Eccentricities are generally in agreement, except for He I lines. Non-He eccentricities are below the previously reported value of 0.63 (Moritani et al. 2018) and support a lower value as also reported in Matchett & van Soelen (2025). The He I abs lines are

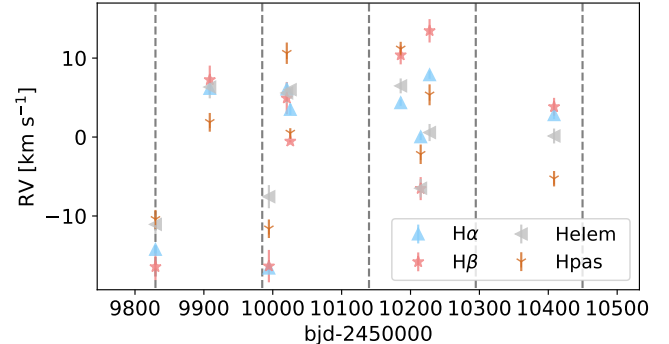


Fig. 4: Radial velocities for EM* VES 826. Vertical dashed lines indicate a 155 d period starting from the first data point.

more in agreement with a value of $e = 0.63$. More data might resolve this discrepancy.

While the signal in the absorption lines is too low to determine robust orbital solutions for systems in group S, it seems that the emission lines do trace the orbital period. Currently, the orbital coverage of both systems in this group is not sufficient to determine orbital periods independently from the X-ray orbital solutions. Nevertheless, the periodograms do show local maxima at the reported orbital periods. With more data, it is possible that these peaks become more significant.

Despite knowing the orbital periods, independent orbital solutions could still not be determined from these data, indicating that a large amount of data are needed to effectively determine orbital solutions for eccentric Be binaries. While this is a natural effect of eccentricity, for Be systems this issue might be more prominent because of the larger intrinsic scatter that can already be present in the RVs.

5.3. Group LV: large-scale emission-line variability

It can be expected that large-scale variability in the emission lines affects the obtained RVs. While this should not affect pure absorption lines (i.e. absorption lines without any contamination from emission), the signal in the absorption lines of the systems in this group is often too weak. We discuss the cases of sub-

Table 3: Orbital solutions for HD 259440 using different spectral lines.

spectral line	P [d]	e	ω [°]	T0	K_1 [km s $^{-1}$]	z_0 [km s $^{-1}$]	rms
H β	317.3 *	0.44 ± 0.13	225 ± 18	9083 ± 11	5.68 ± 0.75	-2.14 ± 0.34	1.5
H α	317.3 *	0.43 ± 0.07	278.6 ± 7.9	9118.9 ± 5.4	8.21 ± 0.64	-0.50 ± 0.30	0.86
OI	317.3 *	0.29 ± 0.17	307 ± 42	9142 ± 37	9.7 ± 3.4	-5.1 ± 1.1	2.6
He I em	317.3 *	0.74 ± 0.64	126 ± 107	9061 ± 14	8.9 ± 9.1	2.8 ± 4.3	2.7
He I abs	317.3 *	0.63 ± 0.10	131 ± 49	9073 ± 16	18.2 ± 3.1	3.7 ± 1.7	5.2
Fe	317.3 *	0.38 ± 0.13	240 ± 16	9102.4 ± 8.4	5.42 ± 0.51	-0.66 ± 0.24	0.75

Notes Listed uncertainties correspond to 1σ . * Fixed to value obtained in Adams et al. (2021).

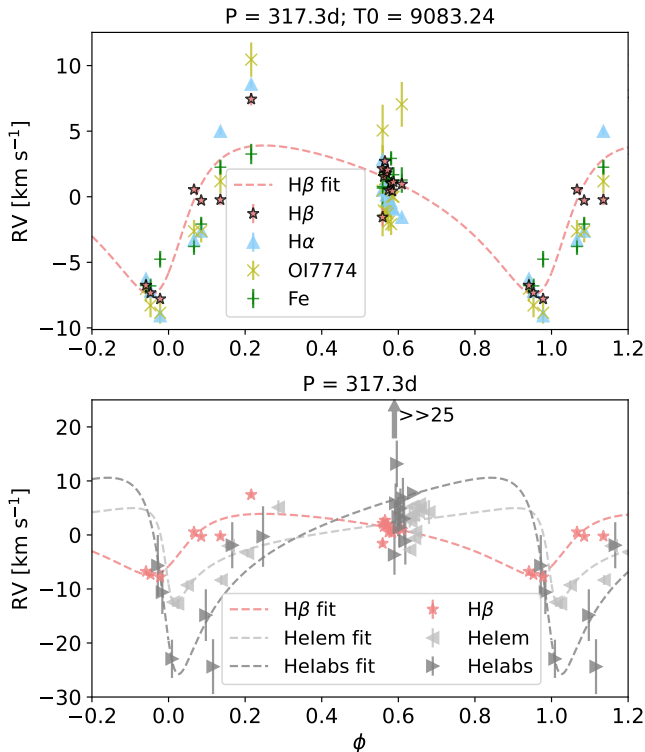


Fig. 5: Phase-folded RVs and fits for HD 259440 on a 317.3 d period. Left panel: RVs from non-He lines and the derived H β RV curve. Right panel: original (not fixed to the T0 of H β) RV fit for He I em and He I abs, with the fit of H β as a reference. The grey arrow indicates a data point with RV > 100 km s $^{-1}$ and falls outside the range of the plot (25 km s $^{-1}$).

divisions LV-vr (extreme V/R variability; V831 Cas) and LV-ls (strong line strength and width variation; V725 Tau, X Per), and discuss V420 Aur separately.

5.3.1. Group LV-vr: extreme V/R variability

In this group we have one system: V831 Cas. The V/R variability is so strong that the emission-line profiles vary from P-Cygni-like to reverse P-Cygni-like (see Fig. A6). Only in H α does the lower peak of the V/R variability never reach the continuum level (in our series of spectra). In such cases, it becomes challenging or almost impossible to exclude the varying top region (i.e. the emission peaks) from the fitting. We can expect that, using the same template for all spectra will result in blue-shifted (red-shifted) RVs for emission-dominated (absorption-dominated) lines in spectra with V/R > 1 compared to spectra with V/R < 1 .

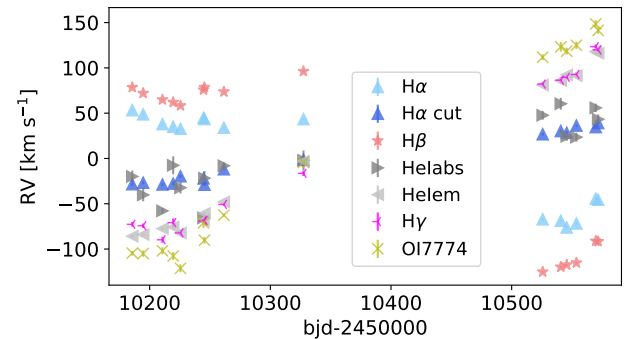


Fig. 6: Non-phase-folded RVs for V831 Cas.

This effect can indeed be seen in Fig. 6. Here, even the He I absorption lines apparently not contaminated by emission (marked by ‘a’ in Table A1 and ‘HeIabs’ in Fig. 6) seem to follow the red-shifted trend upon V/R reversal, even within 5σ . This suggests that they could also be affected by emission, or that the change in V/R is related to true orbital motion. Interestingly, the wings of the H α line (‘H α cut’), which seem to be less variable in shape, appear to follow the trend of the absorption lines. Why the wings of H α would trace the motion of the absorption lines instead of the emission lines is non-trivial.

If the V/R variability and orbital motion are indeed related, the spiral disc density would be created by the passing of the NS, which was shown to be possible through hydrodynamic simulations (Panoglou et al. 2016, 2018). However, it is uncertain if a 1240 d period (Reig et al. 2000) can result in such extreme V/R variability.

A better understanding of disc mechanics and companion-disc interactions (as e.g. in Rubio et al. 2025) is needed to overcome these challenges and draw any conclusions on the orbital periods of systems with extreme V/R variability. Hence, currently, no orbital solution can be derived for these systems.

5.3.2. Group LV-ls: strong non-V/R variability

The targets in this group (V725 Tau and X Per) show strong emission-line variation in both the width and strength of the emission lines, on top of potential V/R variability. Both systems show similar behaviour in their variability. In some spectra, there is a broadening of the emission lines, most apparent in the blue wing. This blue broadening will naturally affect the RVs determined from these spectra. While for V725 Tau the strong line-profile variability could be related to a major outburst, for X Per there is no previous outburst reported. Furthermore, V725 Tau also shows a large decrease in line strength for other spectra post-outburst.

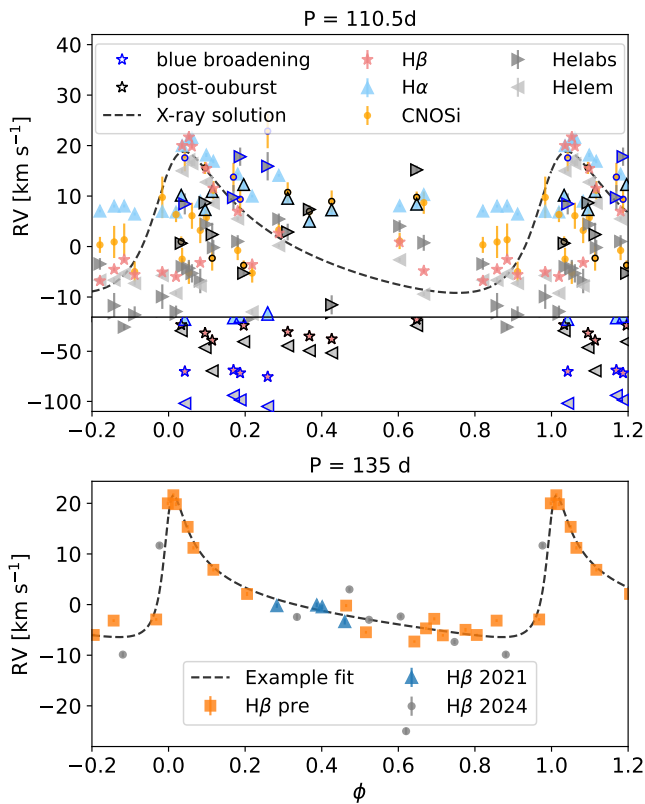


Fig. 7: Phase-folded RVs of V725 Tau. Top: Different spectral lines and orbital solution using the X-ray period and eccentricity (solid black line, $P = 110.5$ d, $e = 0.47$; Finger et al. 1994). Data points with blue edges suffer from blue broadening and black edges represent RVs post-blue broadening and -outburst. The lower panel is a continuity from the upper panel but is differently scaled for clarity. Bottom: Combined $H\beta$ RVs pre- and post-outburst. Orange squares are pre-outburst, blue triangles are 2021 post-outburst (blue broadened), and grey dots are 2024 post-outburst. The dashed line is a by-eye-example orbit with $P = 135$ d and $e = 0.72$.

In Figs. 7 and 8, the RVs measured on spectra with the apparent blue broadening (blue-edged symbols) are much more blue-shifted than the other RVs, as expected. Even absorption-line RVs seem to be affected. For V725 Tau, the other RVs post-outburst (black edged symbols in Fig. 7) also do not follow the RVs pre-outburst. This shows the effect of large-scale variability on the obtained RVs of Be emission lines. Unfortunately, due to the low S/N in the absorption lines, we cannot derive an orbital solution from these RVs either and, for X Per, it seems like the $He\ 1$ absorption lines are also affected.

It becomes challenging to directly combine all data to determine orbital solutions due to large, potentially untrue, RV shifts. Currently, more data is needed to understand if the apparent blue-shift of emission lines is also related to a true RV shift. However, more likely, disc mechanisms (e.g. a spiral density structure or the outburst affecting the disc, ...) are at play.

Therefore, to combine all data, we could split them in parts and use CC on each set of spectra. Then, each set would have a different z_0 and could be scaled to perform a combined fit. An example is shown in Fig. 7 for V725 Tau, where we split the data in pre-outburst, blue broadened spectra post-outburst of 2021, and the other set of spectra taken post-outburst in 2024. This is not a formal fit, but rather an example of a by-eye-fit as

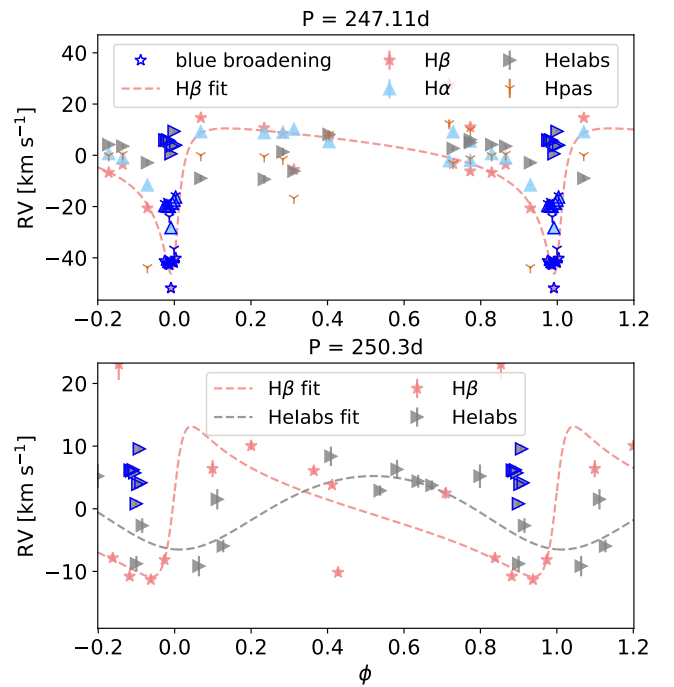


Fig. 8: Phase-folded RVs of X Per. Blue-edged symbols correspond to blue-broadened spectra. Top: on a 247.11 d period, with the fitted RV curve on $H\beta$. Bottom: on a 250.3 d period obtained when excluding the blue-broadened data points from the fit.

the post-outburst data does not cover enough critical parts in the orbit to perform a combined fit.

For X Per, the time-span of the blue-broadened data is only 10 days, so a scaling is not possible. Excluding the blue-broadened RVs from the fitting results in large uncertainties on the obtained parameters (bottom two rows in Table 4). Without fixing the orbital period, it could still be retrieved.

In both cases, the orbital X-ray solution is not retrieved and the absorption lines do not trace the same motion as the emission lines. Thus, also for systems of group LV-Is, determining orbital periods is challenging and a vast amount of data pre- and post-changes is required.

Moreover, for V725 Tau, the motion traced by $H\alpha$ has a smaller semi-amplitude than the one traced by $H\beta$. This shows again that $H\alpha$ is not always a trustworthy tracer of orbital motion. Why this trend is only seen in $H\alpha$ remains unknown.

5.3.3. V420 Aur

V420 Aur does not show the same variability as other systems in the LV group. Only in the final spectra does the emission-line strength seem to change (Fig. A3), but without clear sign of blue broadening or large V/R variability.

The top panel of Fig. 9 shows the non-phase-folded RVs with different spectral lines. Most of the variability for the $He\ 1$ lines and CNOSi blend falls within the estimated precision listed in Table C1 (~ 5 km s $^{-1}$). Hence, apart from the most recent RV measurements in the last frame (i.e. those coinciding with the increase in line strength), not much RV variability is seen.

No orbital period has been reported for V420 Aur. However, the periodograms of the emission lines returned a period of 434.26 ± 6.89 d (top-right panel in Fig. D1). Phase-folded RVs to this period are shown in the bottom

Table 4: Orbital solutions for X Per for different spectral lines.

spectral line	P [d]	e	ω [°]	T0	K_1 [km s ⁻¹]	z_0 [km s ⁻¹]	rms
H β	247.11 ± 0.75	0.78 ± 0.04	216 ± 10	10138.6 ± 5.4	28.3 ± 2.2	-12.0 ± 1.9	8.6
H α	248.13 ± 0.47	0.78 ± 0.04	214.6 ± 9.6	10145.2 ± 3.4	16.8 ± 1.2	6.6 ± 1.1	2.8
H β^r	250.3^*	0.68 ± 0.79	98 ± 83	10359 ± 19	12 ± 23	-6.4 ± 5.5	4.8
He I abs ^r	250.3^*	0.39 ± 0.38	358 ± 52	10435 ± 25	7.7 ± 4.8	-5.2 ± 1.4	3.2

Notes Listed uncertainties correspond to 1σ . ^r Orbital solution with blue broadening RVs removed for fitting. * Fixed to value obtained in Yatabe et al. (2018).

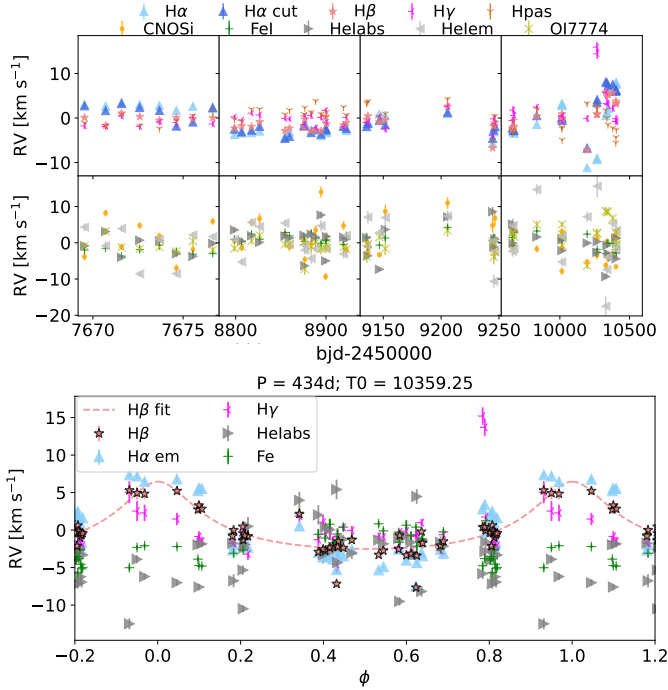


Fig. 9: Top: Non-phase folded RVs for V420 Aur for different spectral lines, split over four panels to exclude large time gaps. Bottom: RVs phase-folded onto a 434 d period and the fit on H β .

panel of Fig. 9 with a tentative orbital solution on H β resulting in $P = 433.6 \pm 3.6$ d, $e = 0.44 \pm 0.12$, $\omega = 359 \pm 15$ °, $T0 = 10359 \pm 15$, $K_1 = 4.5 \pm 1.1$ km s⁻¹, and rms = 1.4.

The strong emission-line (H β , H α , partly H γ) RVs at periastron are those corresponding to the final spectra, for which the line strength increased. Hence, the reliability of the RV change of these data points is questionable. The RVs of He I and Fe (even though it is an emission line) do not follow the motion of the strong emission lines. More data at the suggested periastron passage is needed to confirm or reject the emission-line periodicity.

6. Discussion

In Sect. 6.1 we compare the usage of emission lines and absorption lines. We discuss implications of our derived orbital solutions on the mass function and hence the mass and nature of the companion to the Be star in Sect. 6.2.

6.1. Emission lines vs. absorption lines

On the one hand, strong emission lines like H α and H β show less short-term scatter (i.e. have a smaller σ_{meas}) compared to

weaker or smeared-out lines such as the He I absorption lines (see Sect. 4.2). On the other hand, in some systems, H α does not seem to trace similar motion as other lines (e.g. V725 Tau discussed here or LB-1; Liu et al. 2019; Abdul-Masih et al. 2020). The current cause is unknown, but possible scenarios could be accretion hotspots or the combined motion of an accretion disc around the companion and the Be-star disc. Moreover, in some Be stars, the emission lines show large-scale variability (group LV), which drastically impacts the RV measurements. While absorption lines thus might seem like a better probe, only for two BeXRBs in our sample do absorption lines show periodicity with a larger amplitude than their uncertainties (V615 Cas and HD 259440) and in some other systems (e.g. EM* VES 826), CC could not even converge on the absorption lines. In some systems, it also appears that the apparent He I absorption lines are still contaminated by disc emission (e.g. V831 Cas, Sec. 6.2.4). Hence, in some cases, emission lines are the only measure we have (spectroscopically). Furthermore, the He I absorption lines are more prone to spurious RV measurements (see e.g. RVs in Figs. 3 and 5). In spectra which have a low S/N, no reliable RVs can be obtained in lines with weaker and smeared out signals. Even CC does not obtain uncertainties that could indicate a spurious RV. One of the advantages of using emission lines is thus that spectra with a lower S/N can still be used to measure RVs.

To summarise, neither absorption nor emission lines yield fully optimal results when it comes to detecting orbital motion. Below, we give an overview of our suggestions for which spectral lines to use depending on the goal (see also Fig. 10). For the purpose of determining binary statistics in a population of Be stars or to assess if a specific system is a binary, we suggest using emission lines. Preferably, not the H α line, as it suffers most from variability, but instead H β can be used. While H γ might also be a good tracer, it is more prone to changes from emission dominated to absorption dominated when emission-line strength varies, thus requiring more caution. Assuming most large-scale variability (e.g. V/R variation and blue broadening) is caused by companions, orbital periods can also be determined from the emission lines. This can be done through RV measurements, as shown here, or through the equivalent widths (e.g. Zamanov et al. 2022).

However, to determine accurate orbital solutions, a case-by-case study is preferred. First, one needs to determine if there is large-scale variability. If not, the signal in the emission lines will likely improve the orbital fit compared to the absorption lines. Again, we do advise against using H α . If large-scale variability does show in the spectrum, it is best to rely more on absorption lines, as extreme V/R variability (group LS-vr; e.g. V831 Cas), or blue broadening and outbursts (group LS-lv; e.g. V725 Tau), will induce additional shifts in the RVs.

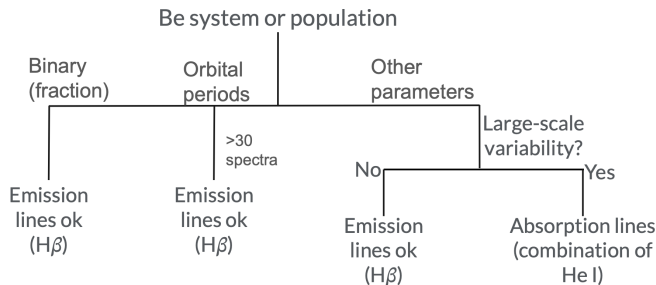


Fig. 10: Schematic overview of our recommendations for the analysis of individual Be stars or populations.

6.2. Discussion of the orbital solutions

From the orbital solutions, we can obtain information on the mass of the unseen companion through the mass function

$$f_m = \frac{m_c^3 \sin^3 i}{(m_{\text{Be}} + m_c)^2} = \frac{PK_{\text{Be}}^3}{2\pi G} (1 - e^2)^{3/2}, \quad (4)$$

where the subscript ‘Be’ and ‘c’ refer to the Be star and companion respectively, and K_{Be} is the derived K_1 of our orbital solutions. By using the Be-star mass and assuming an inclination of 90° , a minimum mass for the companion $M_{c,\text{min}}$ can be obtained. Below, we briefly discuss the mass function and its implications on the nature and masses of the companions for HD 259440, V420 Aur, V615 Cas. For X Per, the uncertainties are too large to obtain a meaningful mass function. We also briefly discuss the RV measurements of V831 Cas.

6.2.1. HD 259440

Using the solution for $\text{H}\beta$ ($P = 317.3$ d, $e = 0.44 \pm 0.13$, $K_1 = 5.68 \pm 0.75$ km s $^{-1}$), we find $f_m = 0.0044 \pm 0.0020 M_\odot$. Assuming $M_{\text{Be}} = 13.2 (19.0) M_\odot$ (Aragona et al. 2010), we obtain $M_{c,\text{min}} = 0.96 \pm 0.15 (1.21 \pm 0.19) M_\odot$, where the errorbars will be slightly underestimated due to fixing the period. Typical NS masses are reached when $25^\circ \lesssim i \lesssim 45^\circ$ ($30^\circ \lesssim i \lesssim 55^\circ$). Lower inclinations would imply a BH companion, while higher inclinations would imply a white dwarf (WD) companion. If the disc and orbit are aligned, the lack of clear absorption features in the hydrogen emission lines would indicate a moderate inclination. For solutions with higher RV semi-amplitudes (e.g. $\text{H}\alpha$: $e = 0.43 \pm 0.07$, $K_1 = 8.21 \pm 0.64$ km s $^{-1}$), f_m becomes $0.0134 \pm 0.0035 M_\odot$ and $M_{c,\text{min}} = 1.42 \pm 0.13 (1.80 \pm 0.16) M_\odot$. In this case, a WD would be ruled out.

6.2.2. V420 Aur

For V420 Aur, the validity of the orbital solution is based on whether we trust the RVs determined from the spectra that have stronger emission lines. If so, the orbital solution for V420 Aur ($P = 433.6 \pm 3.6$ d, $e = 0.44 \pm 0.12$, $K_1 = 4.5 \pm 1.1$ km s $^{-1}$) results in $f_m = 0.0030 \pm 0.0023 M_\odot$. Given the large uncertainty, it is difficult to make any suggestions for the nature of the companion.

6.2.3. V615 Cas

The $\text{H}\beta$ orbital solution ($P = 26.506 \pm 0.003$ d, $e = 0.58 \pm 0.13$, $K_1 = 14.1 \pm 2.6$ km s $^{-1}$) results in $f_m = 0.0041 \pm 0.0027$. V615 Cas is classified as a B0 V star (Grundstrom et al. 2007) and thus we can assume a mass for the Be star between $13.2\text{--}15.5 M_\odot$

(e.g. Janssens et al. 2022). With $M_{\text{Be}} = 13.2 (15.5) M_\odot$, we obtain $M_{c,\text{min}} = 0.94 \pm 0.22 (1.04 \pm 0.24) M_\odot$. The detection of radio pulsations suggests the companion is a NS, and thus a much lower inclination of $i \lesssim 45\text{--}50^\circ$ is necessary. In contrast, the deep absorption or shell features observed in the spectrum indicate an almost edge-on view of the Be disc. This could imply a misalignment of the Be disc and orbital plane, as is suggested by the presence of a precession period.

6.2.4. V831 Cas

Even though no orbital solution could be derived for V831 Cas, the absorption lines show RV variations with a semi-amplitude of ~ 50 km s $^{-1}$. If this would represent true orbital motion, the ~ 1200 d period (Reig et al. 2000) would lead to a minimum mass of the unseen companion $>15 M_\odot$, even for a Be-star mass of $1 M_\odot$ (which would be far too low for its spectral type). Given the pulsar nature of the companion (Haberl et al. 1998; Reig et al. 2000), this orbital solution is thus not possible. Hence, the apparent absorption lines are likely contaminated by the emission component as well.

7. Conclusion

We performed optical spectroscopic analysis of seven BeXRBs. The goal of this work was to compare RVs obtained from different spectral lines and methods against orbital periods and potentially eccentricities obtained from the X-rays.

All three methods (CC, lpf, and bisector) can result in satisfactory results for RV determination. However, CC is more autonomous than lpf and can be used on line blends, unlike the bisector method. The measurements uncertainties of the bisector method are largely underestimated.

The formal precision that can be reached with strong emission lines (e.g. $\text{H}\alpha$: $\sim 0.2\text{--}0.3$ km s $^{-1}$; $\text{H}\beta$: $\sim 0.5\text{--}1.5$ km s $^{-1}$), is better than that of weaker (absorption) lines (e.g. He I : > 3 km s $^{-1}$). Not only is there more variability in the absorption lines due to the lower signal, the pulsations of Be stars add another factor of variability. On top of that, apparent absorption lines can be contaminated by emission. Moreover, emission-line RVs are more robust for spectra with low S/N and less prone to outliers.

Small-scale emission-line variability in the top regions seems to cause minor issues when determining RVs. On the contrary, large-scale variability due to outbursts or V/R variation will significantly affect RV measurements. Therefore, we highlight the need for a vast amount of data. Long-term orbital campaigns can be dedicated to Be stars to monitor the orbital period in between outbursts, to circumvent extreme line-profile variability.

Overall, determining independent orbital periods and solutions for Be stars remains challenging. We make the following suggestions to improve the analysis of Be stars (see also Fig. 10):

- For systems showing stable emission lines (groups A and S), we suggest that the emission lines, in particular $\text{H}\beta$, are reliable RV tracers. The signal in absorption lines of Be stars is often too weak to obtain reliable RVs. Furthermore, we advise against $\text{H}\alpha$ because its motion is known to deviate from that of other spectral lines (e.g. for V725 Tau or LB-1). The cause is currently unknown.
- In case of large-scale variability (group LV) due to outbursts, data pre- and post-outburst can be analysed separately and then combined. For V/R variability, this is not so trivial. If the V/R variability does not cause P-Cygni-like line-profiles,

excluding the variable region (the top) can improve measurements. However, if P-Cygni like profiles occur (e.g. V831 Cas), we currently can only suggest to rely on absorption-line RV measurements.

- The typical criteria that are used to obtain binary fractions should be reconsidered for Be stars, as absorption lines are very prone to outliers. While, emission-lines might be a better probe for the binary statistics, caution needs to be taken about systems showing large-scale variability (group LV).

Without improvements in our understanding of how disc-companion interactions alter the spectral profiles, spectroscopic analysis on Be stars will remain challenging. Therefore, we highly encourage further studies of the mechanics of Be discs (as e.g. in Rubio et al. 2025). More specifically, we need to improve our understanding beyond solely V/R variations, but also how different spectral lines react upon interaction. Indeed, different lines can show different line-profile changes (e.g. for X Per; Fig. A7). This is likely related to how deep in the disc the companion penetrates and the corresponding changing density profile in the disc. Furthermore, we need to understand if these interactions can cause the blue broadening seen in V725 Tau and X Per and if there is a way to correct for this. Both systems might be excellent examples to study this as they show different variability in different spectral lines. With a better understanding of companion-disc interactions, we will be able to further distinguish orbital motion from intrinsic variability.

Data availability

The RV data are only available in electronic format at the CDS via anonymous ftp to cdsarc.u-strasbg.fr (130.79.128.5) or via <http://cdsweb.u-strasbg.fr/cgi-bin/qcat?J/A+A/>.

Acknowledgements. This research has used data obtained at the Mercator Observatory which receives funding from the Research Foundation – Flanders (FWO) (grant agreement I000325N and I000521N). This project has received funding from the FWO PhD fellowships under project 11E1721N, the Postdoctoral International Research Fellowships of Japan Society for the Promotion of Science (Graduate school of Science, Tokyo university), the European Research Council (ERC) under the European Union’s Horizon 2020 research and innovation programme (grant agreements n° 772225/MULTIPLES and 101164755/METAL), from the KU Leuven Research Council (grant METH/24/012), and from the “La Caixa” Foundation (ID 100010434) under the fellowship code LCF/BQ/PI23/11970035. TS acknowledges support from the Israel Science Foundation (ISF) under grant number 0603225041.

References

Abdul-Masih, M., Banyard, G., Bodensteiner, J., et al. 2020, *Nature*, 580, E11

Adams, C. B., Benbow, W., Brill, A., et al. 2021, *ApJ*, 923, 241

Aragona, C., McSwain, M. V., & De Becker, M. 2010, *ApJ*, 724, 306

Aragona, C., McSwain, M. V., Grundstrom, E. D., et al. 2009, *ApJ*, 698, 514

Baade, D. 1987, in IAU Colloq. 92: Physics of Be Stars, ed. A. Slettebak & T. P. Snow, 361

Baade, D. & Balona, L. A. 1994, in IAU Symposium, Vol. 162, Pulsation; Rotation; and Mass Loss in Early-Type Stars, ed. L. A. Balona, H. F. Henrichs, & J. M. Le Contel, 311

Bevington, P. R. & Robinson, D. K. 2003, Data Reduction and Error Analysis for the Physical Sciences, 3rd ed. (McGraw-Hill)

Bjorkman, K. S., Miroshnichenko, A. S., McDavid, D., & Pogrosheva, T. M. 2002, *ApJ*, 573, 812

Bodensteiner, J., Shenar, T., Mahy, L., et al. 2020a, *A&A*, 641, A43

Bodensteiner, J., Shenar, T., & Sana, H. 2020b, *A&A*, 641, A42

Bongiorno, S. D., Falcone, A. D., Stroh, M., et al. 2011, in AAS/High Energy Astrophysics Division, Vol. 12, AAS/High Energy Astrophysics Division #12, 13.20

Bouber, D. & Evans, N. W. 2018, *MNRAS*, 477, 5261

Casares, J., Ribas, I., Paredes, J. M., Martí, J., & Allende Prieto, C. 2005, *MNRAS*, 360, 1105

Casares, J., Ribó, M., Ribas, I., et al. 2012, *MNRAS*, 421, 1103

Chojnowski, S. D., Labadie-Bartz, J., Rivinius, T., et al. 2018, *ApJ*, 865, 76

Clark, J. S., Lyuty, V. M., Zaitseva, G. V., et al. 1999, *MNRAS*, 302, 167

Coe, M. J., Reig, P., McBride, V. A., Galache, J. L., & Fabregat, J. 2006, *MNRAS*, 368, 447

D’Ai, A., Cusumano, G., La Parola, V., Segreto, A., & Mineo, T. 2016, *MNRAS*, 456, 1955

Dallas, M. M., Oey, M. S., & Castro, N. 2022, *ApJ*, 936, 112

Delgado-Martí, H., Levine, A. M., Pfahl, E., & Rappaport, S. A. 2001, *ApJ*, 546, 455

Dhawan, V., Mioduszewski, A., & Rupen, M. 2006, in VI Microquasar Workshop: Microquasars and Beyond, 52.1

Doazan, V., Marlborough, J. M., Morossi, C., et al. 1986, *A&A*, 158, 1

Dodd, J. M., Oudmaijer, R. D., Radley, I. C., Vioque, M., & Frost, A. J. 2024, *MNRAS*, 527, 3076

Dsilva, K., Shenar, T., Sana, H., & Marchant, P. 2020, *A&A*, 641, A26

Dufont, P. L., Lennon, D. J., Villaseñor, J. I., et al. 2022, *MNRAS*, 512, 3331

Fabry, M., Hawcroft, C., Mahy, L., et al. 2021, spinOS: SPectroscopic and INterferometric Orbital Solution finder, Astrophysics Source Code Library, record ascl:2102.001

Falcone, A. D., Grube, J., Hinton, J., et al. 2010, *ApJ*, 708, L52

Ferrigno, C., Farinelli, R., Bozzo, E., et al. 2013, *A&A*, 553, A103

Finger, M. H., Cominsky, L. R., Wilson, R. B., Harmon, B. A., & Fishman, G. J. 1994, in American Institute of Physics Conference Series, Vol. 308, The Evolution of X-ray Binaries, ed. S. Holt & C. S. Day (AIP), 459

Finger, M. H., Wilson, R. B., & Harmon, B. A. 1996, *ApJ*, 459, 288

Fortin, F., García, F., Simaz Bunzel, A., & Chaty, S. 2023, *A&A*, 671, A149

Giangrande, A., Giovannelli, F., Bartolini, C., Guarneri, A., & Piccioni, A. 1980, *A&AS*, 40, 289

Gies, D. R., Fullerton, A. W., Bolton, C. T., et al. 1994, *ApJ*, 422, 823

Grundstrom, E. D., Caballero-Nieves, S. M., Gies, D. R., et al. 2007, *ApJ*, 656, 437

Haberl, F., Angelini, L., & Motch, C. 1998, *A&A*, 335, 587

Haigh, N. J., Coe, M. J., & Fabregat, J. 2004, *MNRAS*, 350, 1457

Hastings, B., Langer, N., Wang, C., Schootemeijer, A., & Milone, A. P. 2021, *A&A*, 653, A144

Hutchings, J. B. 1984, *PASP*, 96, 312

Hutchings, J. B. & Crampton, D. 1981, *PASP*, 93, 486

Janssens, S., Shenar, T., Degenaar, N., et al. 2023, *A&A*, 677, L9

Janssens, S., Shenar, T., Sana, H., et al. 2022, *A&A*, 658, A129

Jaschek, M. & Egret, D. 1995, VizieR Online Data Catalog: Catalogue of Be stars (Jaschek+, 1982), VizieR On-line Data Catalog: III/67A. Originally published in: 1982IAUS...98..261J

Klement, R., Rivinius, T., Gies, D. R., et al. 2024, *ApJ*, 962, 70

Koubeký, P., Kotková, L., Votruba, V., Šlechta, M., & Dvořáková, Š. 2012, *A&A*, 545, A121

Kravtsov, V., Berdyugin, A. V., Piironen, V., et al. 2020, *A&A*, 643, A170

La Palombara, N., Sidoli, L., Esposito, P., Tiengo, A., & Mereghetti, S. 2012, *A&A*, 539, A82

Labadie-Bartz, J., Chojnowski, S. D., Whelan, D. G., et al. 2018, *AJ*, 155, 53

Larionov, V., Lyuty, V. M., & Zaitseva, G. V. 2001, *A&A*, 378, 837

Liu, J., Zhang, H., Howard, A. W., et al. 2019, *Nature*, 575, 618

Liu, Q. Z., van Paradijs, J., & van den Heuvel, E. P. J. 2000, *A&AS*, 147, 25

Lomb, N. R. 1976, *Ap&SS*, 39, 447

López-Miralles, J., Motta, S. E., Migliari, S., & Jaron, F. 2023, *MNRAS*, 523, 4282

Lyubimkov, L. S., Rostopchin, S. I., Roche, P., & Tarasov, A. E. 1997, *MNRAS*, 286, 549

Massi, M. & Jaron, F. 2013, *A&A*, 554, A105

Massi, M., Migliari, S., & Chernyakova, M. 2017, *MNRAS*, 468, 3689

Massi, M. & Torricelli-Ciamponi, G. 2016, *A&A*, 585, A123

Matchett, N. & van Soelen, B. 2025, *MNRAS*, 536, 166

Moritani, Y., Kawano, T., Chimasu, S., et al. 2018, *PASJ*, 70, 61

Moritani, Y., Nogami, D., Okazaki, A. T., et al. 2010, *MNRAS*, 405, 467

Motch, C., Haberl, F., Dennerl, K., Pakull, M., & Janot-Pacheco, E. 1997, *A&A*, 323, 853

Motch, C., Stella, L., Janot-Pacheco, E., & Mouchet, M. 1991, *ApJ*, 369, 490

Nakajima, M., Negoro, H., Mihara, T., et al. 2022, The Astronomer’s Telegram, 15835, 1

Nazé, Y., Rauw, G., Czesla, S., Smith, M. A., & Robrade, J. 2022, *MNRAS*, 510, 2286

Newville, M., Stensitzki, T., Allen, D. B., & Ingargiola, A. 2014, LMFIT: Non-Linear Least-Square Minimization and Curve-Fitting for Python

Okazaki, A. T. 1991, *PASJ*, 43, 75

Panoglou, D., Carciofi, A. C., Vieira, R. G., et al. 2016, *MNRAS*, 461, 2616

Panoglou, D., Faes, D. M., Carciofi, A. C., et al. 2018, *MNRAS*, 473, 3039

Papitto, A., Torres, D. F., & Rea, N. 2012, *ApJ*, 756, 188

Percy, J. R., Harlow, C. D. W., & Wu, A. P. S. 2004, *PASP*, 116, 178

Peters, G. J., Gies, D. R., Grundstrom, E. D., & McSwain, M. V. 2008, *ApJ*, 686, 1280

Poeckert, R. 1981, PASP, 93, 297

Polcaro, V. F., Rossi, C., Giovannelli, F., et al. 1990, A&A, 231, 354

Porter, J. M. & Rivinius, T. 2003, PASP, 115, 1153

Priedhorsky, W. C. & Terrell, J. 1983, Nature, 303, 681

Punsly, B. 1999, ApJ, 519, 336

Raskin, G., van Winckel, H., Hensberge, H., et al. 2011, A&A, 526, A69

Reig, P. 2011, Ap&SS, 332, 1

Reig, P., Negueruela, I., Coe, M. J., et al. 2000, MNRAS, 317, 205

Reig, P., Negueruela, I., Fabregat, J., Chatto, R., & Coe, M. J. 2005, A&A, 440, 1079

Rivinius, T., Baade, D., Hadrava, P., Heida, M., & Klement, R. 2020, A&A, 637, L3

Rivinius, T., Carciofi, A. C., & Martayan, C. 2013, A&A Rev., 21, 69

Rosenberg, F. D., Eyles, C. J., Skinner, G. K., & Willmore, A. P. 1975, Nature, 256, 628

Rossi, C., Norci, L., & Polcaro, V. F. 1991, A&A, 249, L19

Rubio, A. C., Carciofi, A. C., Bjorkman, J. E., et al. 2025, A&A, 698, A309

Saha, A. & Vivas, A. K. 2017, AJ, 154, 231

Sarty, G. E., Kiss, L. L., Huziak, R., et al. 2009, MNRAS, 392, 1242

Scargle, J. D. 1982, ApJ, 263, 835

Schürmann, C., Xu, X. T., Langer, N., et al. 2025, A&A, submitted, arXiv:2503.23878

Shenar, T., Bodensteiner, J., Abdul-Masih, M., et al. 2020, A&A, 639, L6

Stellingwerf, R. F. 1978, ApJ, 224, 953

Struve, O. 1931, ApJ, 73, 94

Taylor, A. R. & Gregory, P. C. 1982, ApJ, 255, 210

Tsygankov, S., Lutovinov, A., & Krivonos, R. 2011, The Astronomer's Telegram, 3137, 1

Tsygankov, S. S., Krivonos, R. A., & Lutovinov, A. A. 2012, MNRAS, 421, 2407

Usui, R., Morii, M., Kawai, N., et al. 2012, PASJ, 64, 79

van den Eijnden, J., Rouco Escorial, A., Alfonso-Garzón, J., et al. 2024, MNRAS, 527, 4260

Virtanen, P., Gommers, R., Oliphant, T. E., et al. 2020, Nature Methods, 17, 261

Štefl, S., Okazaki, A. T., Rivinius, T., & Baade, D. 2007, in Astronomical Society of the Pacific Conference Series, Vol. 361, Active OB-Stars: Laboratories for Stellare and Circumstellar Physics, ed. A. T. Okazaki, S. P. Owocki, & S. Stefl, 274

Štefl, S., Rivinius, T., Carciofi, A. C., et al. 2009, A&A, 504, 929

Walter, R., Lutovinov, A. A., Bozzo, E., & Tsygankov, S. S. 2015, A&A Rev., 23, 2

Weng, S.-S., Qian, L., Wang, B.-J., et al. 2022, Nature Astronomy, 6, 698

White, N. E., Mason, K. O., Sanford, P. W., & Murdin, P. 1976, MNRAS, 176, 201

Wisniewski, J. P., Draper, Z. H., Bjorkman, K. S., et al. 2010, ApJ, 709, 1306

Wu, Y. W., Torricelli-Ciamponi, G., Massi, M., et al. 2018, MNRAS, 474, 4245

Yan, J., Zhang, P., Liu, W., & Liu, Q. 2016, AJ, 151, 104

Yatake, F., Makishima, K., Mihara, T., et al. 2018, PASJ, 70, 89

Zamanov, R., Stoyanov, K. A., Wolter, U., Marchev, D., & Petrov, N. I. 2019, A&A, 622, A173

Zamanov, R. K., Stoyanov, K. A., Marchev, D., et al. 2022, Astronomische Nachrichten, 343, e24019

Zamanov, R. K., Stoyanov, K. A., Martí, J., et al. 2016, A&A, 593, A97

Zucker, S. 2003, MNRAS, 342, 1291

Appendix A: Short description of targets

For each of the seven targets analysed in this work, a small overview is given below, which focuses on previously reported (orbital) periods and eccentricities⁵. We also describe the spectral appearance, including violet-to-red (V/R) variation, where $V/R > 1$ means that the violet or blue wing dominates and $V/R < 1$ indicates that the red wing is dominating. A $V/R \approx 1$ corresponds to a double-peaked profile where the blue and red wing are about equally strong. An overview of the nature of important spectral lines used in this work is also listed in Table A1.

Appendix A.1: EM* VES 826

EM* VES 826 (LS V +44 17, RX J0440.9+4431) contains a B0.2 Ve star (Reig et al. 2005) and is not listed in the BESS database. It was first proposed to be a Be-X-ray binary by Motch et al. (1997) and was listed as a persistent X-ray binary with a pulse period of $P_{\text{puls}} \sim 205$ s (La Palombara et al. 2012; Ferrigno et al. 2013). An orbital period of $P \sim 150 - 155$ d was also estimated from the X-rays (Tsygankov et al. 2012; Usui et al. 2012; Ferrigno et al. 2013). It is one of the three BeXRBs with radio counterparts (van den Eijnden et al. 2024).

EM* VES 826 is also known to have X-ray outbursts in 2011 and 2022-2023 (see Tsygankov et al. 2011; Nakajima et al. 2022, and related telegrams). Spectroscopic monitoring around the 2011 outburst showed that the outburst might be connected with the size of the circumstellar disc, which was largest during the outburst and decreased right after the outburst (Yan et al. 2016). Furthermore, long spectroscopic monitoring suggest an eccentricity ≥ 0.4 (Yan et al. 2016).

For EM* VES 826 we acquired nine epoch spectra, taken between September 2022 and March 2024. In these spectra, EM* VES 826 looks quite different than in the ones shown in Reig et al. (2005). Both $H\alpha$ and $H\beta$ are still clear double peaked emission lines and have remained quite stable. However, $H\gamma$ also shows an emission core, which seems absent in Reig et al. (2005). The $He\ 1$ absorption lines seem weaker now compared to their spectra and some are even seen in emission. Both the CNOSi line blend and $He\ 2$ lines are seen in absorption, while some $He\ 1$ lines are in emission. $Fe\ 2$ emission lines seem to be absent. A typical spectrum is shown in Fig. A1.

Even though the spectral resolution of the data in Reig et al. (2005) is lower (5000-10000) than the Mercator data, the differences in spectral appearance are most likely related to the intrinsic variability of the disc and timing (pre- or post-outburst) of the observations.

Appendix A.2: HD 259440

HD 259440 (EM* MWC 148, LS VI +05 11) hosts a B0pe star (Jaschek & Egret 1995), which has an estimated mass between $13.2 - 19.0 M_{\odot}$ (Aragona et al. 2010). It shows periodic γ -ray and X-ray outbursts. No pulse period has been reported in the literature. The binary nature was first suggested by Falcone et al. (2010) based on the X-ray spectrum. Several studies have later reported a period of ~ 317 d derived from the γ -ray and X-ray data (Bongiorno et al. 2011; Moritani et al. 2018; Adams et al. 2021). Based on RV measurements of the $H\alpha$ emission line, a similar period was derived with a high eccentricity of ~ 0.6 (Moritani et al. 2018), much smaller than the previously re-

ported ~ 0.83 (Casares et al. 2012). Based on the mass function, Moritani et al. (2018) suggested that the companion is a NS with $M \leq 2.5 M_{\odot}$.

For HD 259440, the first 26 spectra were taken in November 2009 for eight consecutive days. Each night, two to three consecutive exposures of 1800s were taken. An additional 12 spectra were obtained between October 2020 and March 2024.

The overall spectral shape is not extremely variable over the observation time base. The $H\alpha$ line is weakly double peaked, but $H\beta$ and other emission lines clearly are double peaked. While $H\alpha$ shows variability in the top, sometimes even becoming single peaked, $H\beta$ shows much less variability. $He\ 1$ lines seem to be absent and most $He\ 1$ lines are in absorption. $Fe\ 2$ emission lines are present throughout the whole spectrum, especially within the region of 5150-5380Å. Interestingly, HD 259440 shows stronger emission in $Ca\ 2\ \lambda\lambda 8498, 8542, 8662$ than the H Paschen emission lines. This line is also seen in other Be systems, where the companion is a hot subdwarf (e.g. *o* Pup Koubek et al. 2012 and HD 55606 Chojnowski et al. 2018). The typical spectrum is shown in Fig. A2.

Appendix A.3: V420 Aur

V420 Aur (HD 34921) was first suggested to be the optical counterpart of the X-ray source 4U 0515+38 by Polcaro et al. (1990). A year later, Rossi et al. (1991) reported on short (300s) time-scale variability in the equivalent width of the $H\alpha$ emission line and Percy et al. (2004) report a 0.8d variability period based in *Hipparcos* photometry. The spectral type of the Be optical component in the system is B0 IV pe (Polcaro et al. 1990). Other than that, not much information can be found in the literature about periodic variability or orbital periods.

For V420 Aur, the first 142 spectra were taken in October 2016 for eight consecutive nights with 10-15 consecutive spectra per night with 120s exposure times. The remaining 45 epochs were taken between November 2019 and March 2024.

The $H\alpha$, $H\beta$, and $H\gamma$ emission lines are double peaked. Almost all $He\ 1$ lines are in absorption. Some are entangled with $Fe\ 2$ emission lines, which are present throughout the whole spectrum, especially within the region of 5150-5380Å. The $O\ 1\ \lambda\lambda 7772, 7774, 7775$ line is in emission and CNOSi in absorption. An $Fe\ 2$ emission line is also seen in the bluest part of this line blend. No $He\ 2$ lines are seen. There is also emission in $Ca\ 2\ \lambda\lambda 8498, 8542, 8662$. However, in contrast to HD 259440, it is not stronger than the H Paschen lines.

The spectra appear variable in the blocks they have been taken. There are four time blocks in which spectra are taken: 2016, 2020, 2023, and 2024. There seems to be V/R variability on time scales of years and also the emission-line strength or width varies per block of observations. Between 2016 and 2020, the emission line width has decreased. Then, in 2023 and 2024, the emission line strength increased. However, the increase is not seen in every spectral line. For example, $H\alpha$ is clearly affected, but $O\ 1\ \lambda\lambda 7772, 7774, 7775$ seems much less affected (apart from in 2023). This can all be seen in Fig. A3.

Appendix A.4: V615 Cas

V615 Cas (LS I +61 303) hosts a B0 V star (Grundstrom et al. 2007). It is detected as an X-ray, radio, and γ -ray source. It has

⁵ For an overview of the high-energy aspects of the sources, the reader is referred to the listed references and references therein.

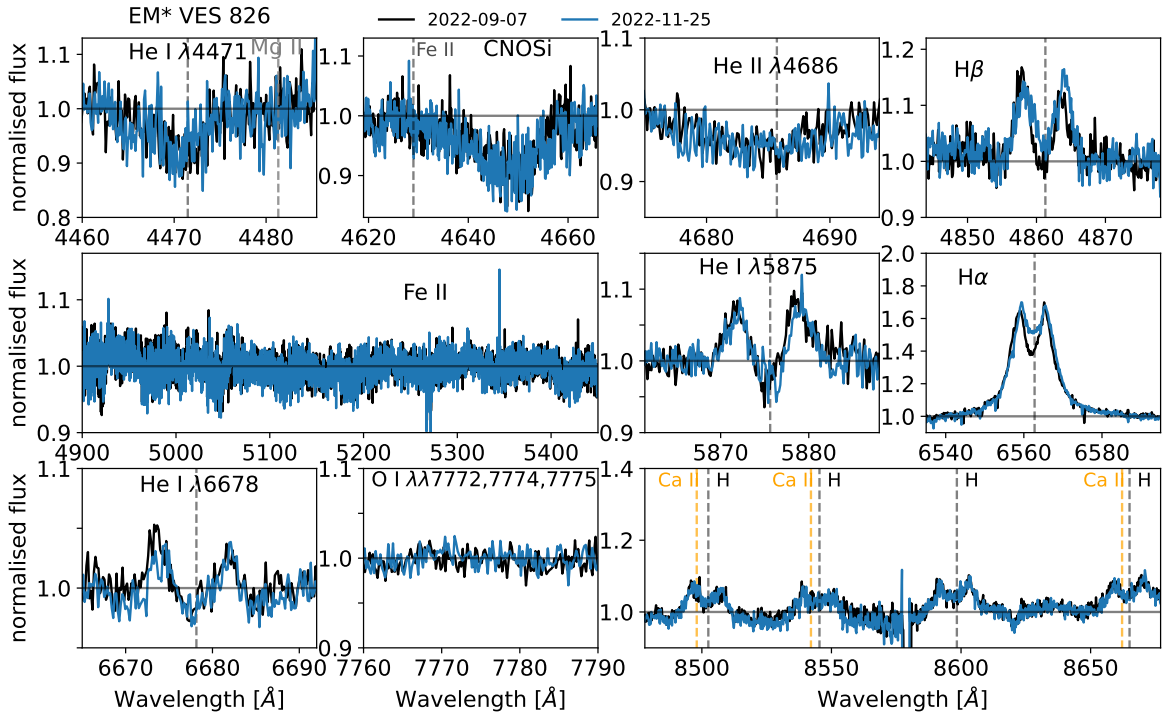


Fig. A1: Spectra for EM* VES 826. The two spectra shown are the first (black) and second (blue) spectra taken, estimated to have the largest RV variability (see Fig. 4).

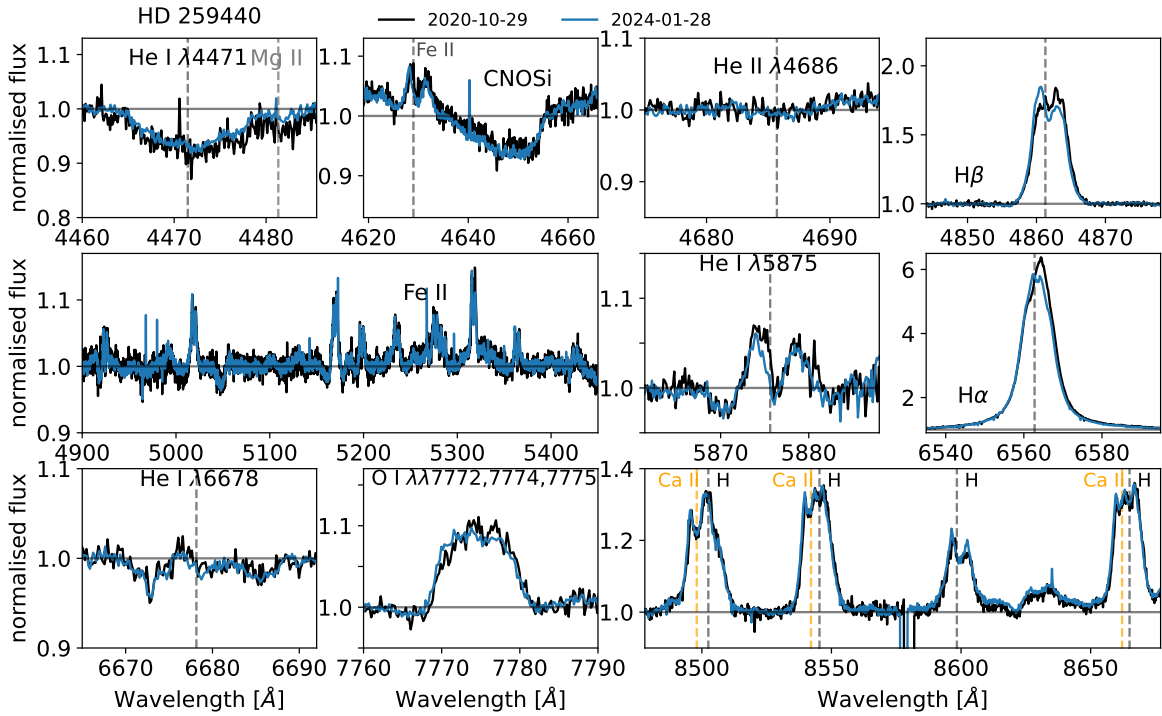


Fig. A2: Spectra for HD 259440. The two spectra shown represent one spectrum close to periastron (blue) and one which is not (black, see Sect. 5.2).

been suggested to be a microquasar with a BH of $\sim 4M_{\odot}$ (Punsly 1999), which could be supported by the X-ray data (Massi et al. 2017). However, a recent study discovered radio pulsations with a period $P_{\text{spin}} = 269$ ms (Weng et al. 2022), indicating a spinning NS in the system. This was already suggested by multiple studies (e.g. Dhawan et al. 2006; Papitto et al. 2012).

The orbital period of ~ 26.5 d is confirmed by several independent studies in different high-energy bands (e.g. Hutchings & Crampton 1981; Taylor & Gregory 1982; D'Aì et al. 2016; López-Miralles et al. 2023) and also through the equivalent width of the H α line (Zamanov et al. 2016). An eccentricity of 0.537 ± 0.034 was reported by Aragona et al. (2009), in line

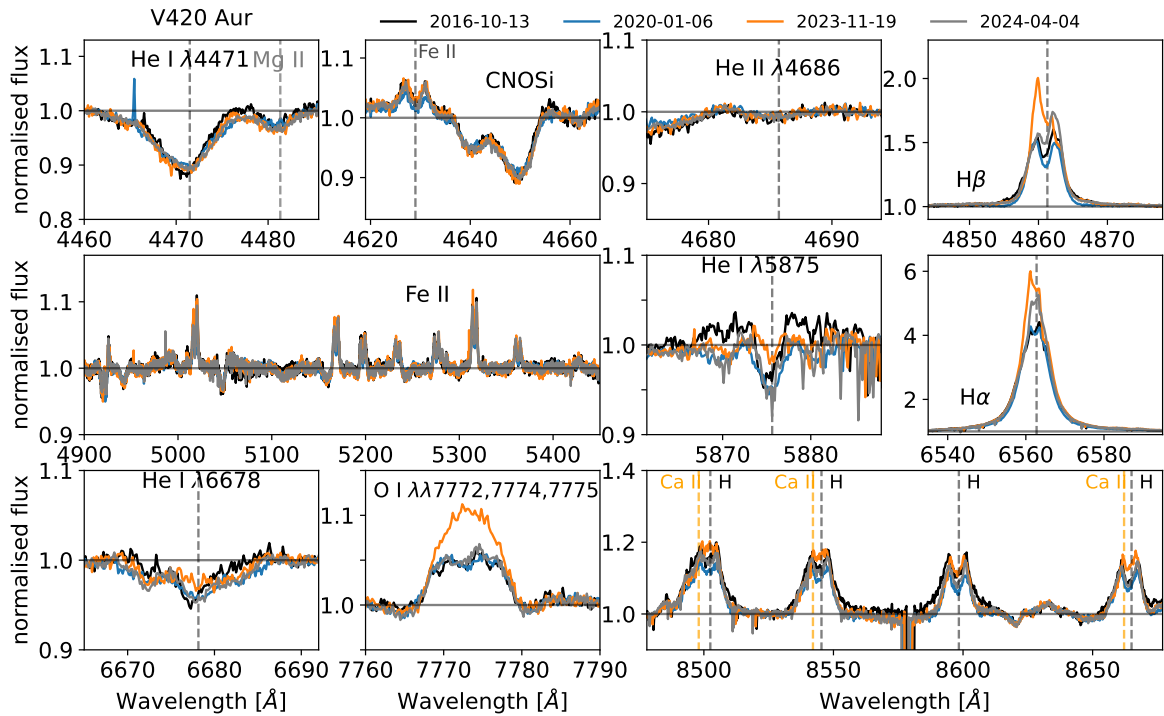


Fig. A3: Three spectra of V420 Aur, taken in different years (see legend).

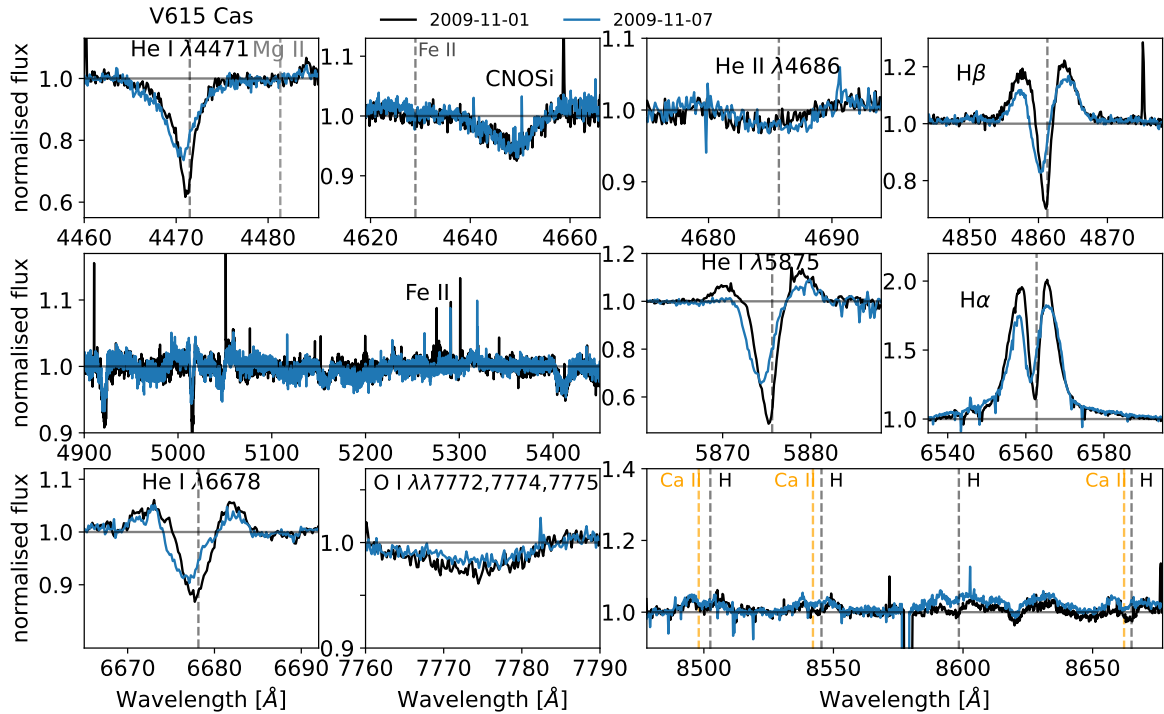


Fig. A4: Spectra of V615 Cas at RV extremes. The black spectrum is close to periastron passage.

with the one reported by [Casares et al. \(2005\)](#) ($e = 0.63 \pm 0.11$). However, based on polarimetry of the disc, the eccentricity is suggested to be much smaller ($e < 0.15$; [Kravtsov et al. 2020](#)). Furthermore, the system is known to have a precession period of ~ 26.9 d, discovered in different data (e.g. [Massi & Jaron 2013](#); [D'Ai et al. 2016](#); [Wu et al. 2018](#)). The proximity of the precession period to the orbital period leads to apparent periods or beat periods of 26.7 d and 1667 d (e.g. [Massi & Jaron 2013](#); [Massi & Torricelli-Ciamponi 2016](#)).

For V615 Cas, the first 21 spectra were taken in November 2009, with three consecutive 1800s exposures per night, thus covering 7 nights. Furthermore, 25 epoch spectra were taken between August 2022 and March 2024, where the final 16 were taken two to three nights apart over a time span of 60 days (about two orbital periods), one more spectrum was obtained in November 2024. All emission lines present in the spectra of V615 Cas are double peaked and their absorption core is very strong. There is some

V/R variability seen over a time span of 15 years. The absorption cores show clear motion (see Fig. A4).

Emission lines belonging to Fe II or the H Paschen series are only weakly present. Most He I lines are in absorption, as is the O I $\lambda\lambda 7772, 7774, 7775$ line. He II lines are also present in absorption. The CNOSi blend appears rather weak and is dominated by noise in some of the spectra.

Interestingly, the absorption lines and the absorption cores of the emission lines seem to become stronger near periastron (blue spectrum in Fig. A4). In a double luminous-star binary, this would be an effect of light of one star being blocked as they move in front of one another. However, for V615 Cas, the only two light sources are the Be star and the disc. Hence, the increase in absorption-line strength could be an effect of the disc being truncated at periastron as the NS companion moves through the disc.

Appendix A.5: V725 Tau

V725 Tau (HD 245770, A 0535+26) consists of a O9.5 III star (Giangrande et al. 1980) and a 104s X-ray pulsar (Rosenberg et al. 1975). Several independent groups (Priedhorsky & Terrell 1983; Finger et al. 1994; Coe et al. 2006) have derived a period of 110-111 d based on X-ray outburst data, while Motch et al. (1991) also confirmed this period with equivalent width measurements of H β . Finger et al. (1994) derived an eccentricity of 0.47. By fixing the orbital period, Hutchings (1984) showed that spectroscopic data agrees with the 111 d period, while reporting an eccentricity of ~ 0.3 .

Photometric analysis did not confirm the 111 d period. However, Clark et al. (1999) showed clear evidence for a a 103 d and 1400 d period in the optical light curve. Larionov et al. (2001) attributed these periodicities to a disc precessing in a 1400 d period, which, combined with the 111 d orbital period, would result in the 103 d beat period seen in the light curves. It is believed that the precessing disc is the tilted Be decretion disc and does not support evidence for a NS accretion disc (Haigh et al. 2004). Furthermore, a 500 d periodicity is detected in the V/R variations of V725 Tau (Moritani et al. 2010), which is attributed to a one-armed density wave in the disc.

V725 Tau underwent a major X-ray and radio outburst in November 2020 (see e.g. this telegram), which is after the first 17 spectra were taken. All other spectra are taken after January 2021 and thus after the major outburst. Furthermore, V725 Tau is reported to have had several major X-ray outbursts starting from 1994 (see related telegrams and Finger et al. 1996).

For V725 Tau, 22 spectra are available. Of those, 17 spectra were taken before the 2020 outburst in November 2019 to March 2020, four were taken a few months after the outburst (January and February 2021), and the other eight were taken between March 2022 and April 2024.

The spectra of V725 Tau are very variable over the 5 yr time period of the observations (see Fig. A5). In the most recent spectra of 2024, the emission lines are much weaker than in earlier ones, which causes, for example, the emission in H γ to dominate the line in the earliest spectra and only be present in the core of the absorption line in the ones of 2024. There is also clear V/R variation. Moreover, in the spectra of 2021, all emission lines either seem to have blueshifted or part of the red wing is no longer visible (which we deem more likely). This phenomenon also coincides with those spectra that have V/R < 1 (i.e. a stronger red emission, than blue) and the first ones taken right after the 2020 outburst (January and February 2021), while the spectra

of 2019 have V/R > 1 and those of 2022 and later show V/R ≈ 1 . Unfortunately, our spectra do not cover the period between March 2021 and March 2022, such that the change in V/R seems rather abrupt in our data set. However, this is not necessarily the true case.

The absorption lines of He I and CNOSi are clearly present and He II absorption is also observed. Fe II emission lines are rather weakly present.

Appendix A.6: V831 Cas

The Be star in V831 Cas (LS I +61 235, RX J0146.9+6121) has a B1 IIIe spectral type (Motch et al. 1997). It is known to be the slowest pulsar, with a pulse period ~ 1400 s (Haberl et al. 1998; Reig et al. 2000).

Sarty et al. (2009) found three photometric periods less than a day, which they attributed to stellar oscillations from the Be star and its spin period. Furthermore, infrared and optical spectroscopy revealed the presence of a one-armed density wave in the Be disc with a period of 1240 d (Reig et al. 2000), which causes strong V/R variations. No orbital period has been reported yet.

For V831 Cas, the 15 epoch spectra were obtained between August 2023 and September 2024. These spectra show clear V/R variability over the course of one year (see Fig. A6). The extend of the variability is large enough to make all emission lines (including He I and O I $\lambda\lambda 7772, 7774, 7775$), except H α , change shapes from an apparent P-cygni profile to an apparent reverse P-cygni profile (i.e. a mirror flip of the spectral lines) over the one-year baseline of the spectra. Almost all He I lines show emission. There are Fe II emission lines are weakly present and He II absorption lines seem absent.

In the most recent spectra (August and September 2024, orange and grey), the H α and H β profiles are distorted, with not only a V/R $>> 1$, but also a triple-peaked emission profile. According to Štefl et al. (2007), this occurs in the transition period from V/R > 1 to V/R < 1 , which could indeed be the case here.

Appendix A.7: X Per

X Per (HD 24534, 4U 0352+30) is not listed in BESS. It is a persistent X-ray binary with a B0/1 Ve luminous component (Lyubimkov et al. 1997; Zamanov et al. 2019) and an X-ray pulse period of 837 s (e.g. White et al. 1976; Haberl et al. 1998). From a pulse-time analysis, Delgado-Martí et al. (2001) derived an orbital period of 250.3 ± 0.6 d and an eccentricity of 0.11. Yababe et al. (2018) estimated a NS mass of around $2M_{\odot}$ from a fitting of the relation between the period change and the bolometric luminosity of the X-ray emitting companion.

For X Per, the first three spectra are taken between 2012 and 2014, with almost one year apart. Then, eight spectra were taken on consecutive nights in October 2018. The last nine spectra were taken between August 2022 and March 2024.

The spectra of X Per are very variable, especially in V/R variability and line strength. Almost all He I lines have emission line contamination. The He II are clearly present in absorption. The CNOSi blend seems to be either not fully blended or to have an emission core. There are also Fe I emission lines present. There seems to be no presence of Ca II $\lambda\lambda 8498, 8542, 8662$ emission lines. Spectra are shown in Fig. A7.

From a visual inspection of the spectra, the emission lines seem

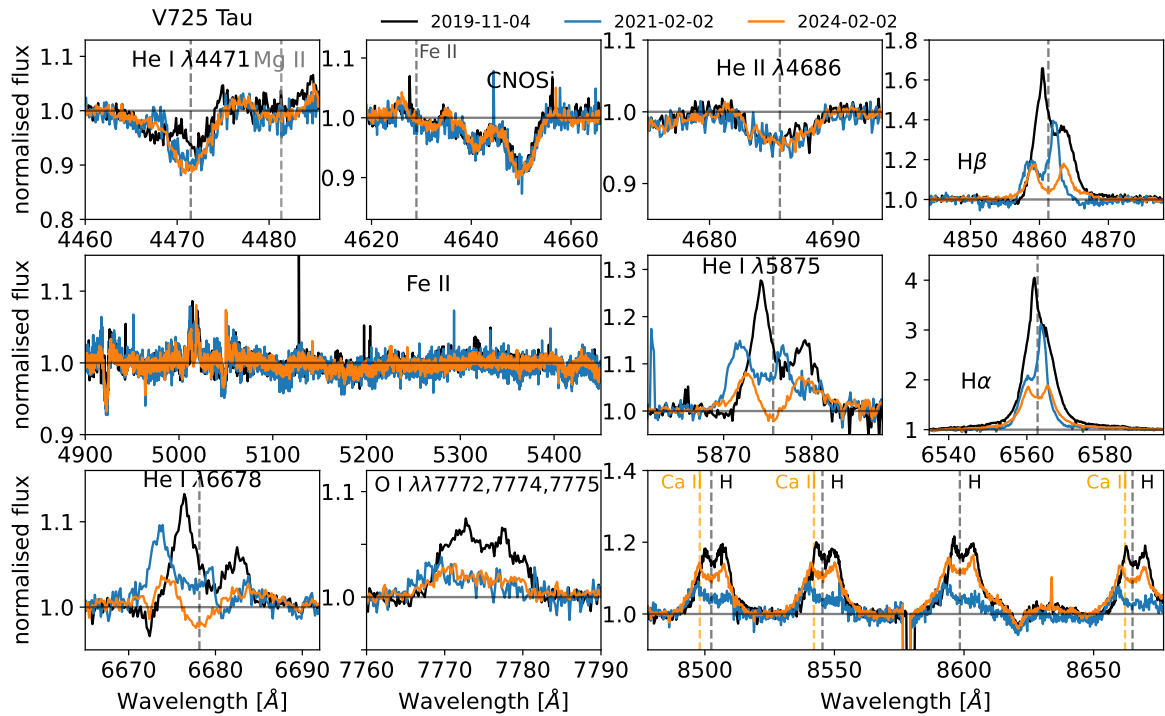


Fig. A5: Spectra for V725 Tau. The black spectrum was taken before the 2020 outburst, the blue one close after the outburst, and the orange one years after the outburst.

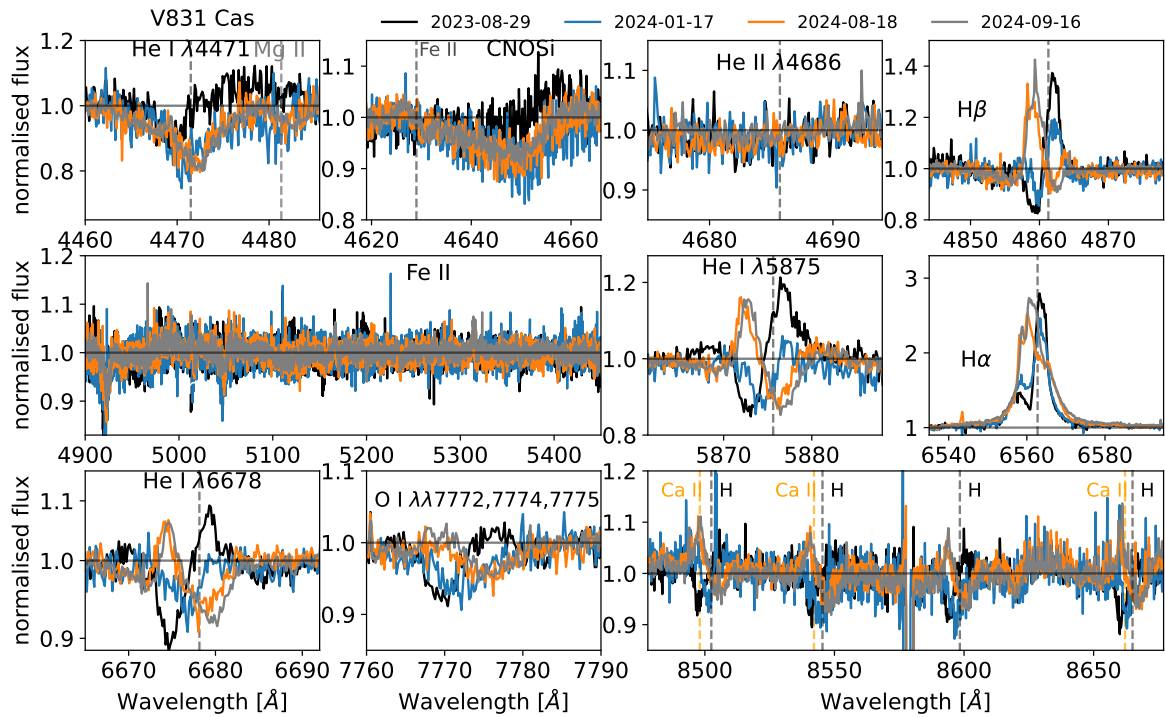


Fig. A6: Spectra of V831 Cas showing clear V/R variability over the course of one year.

to be very variable in the blue wing, but much less so in the red wing. This effect seems less prominent in $H\alpha$, but is strongly present in weaker lines, such as the He I lines. This will make it difficult to distinguish between disc variability and orbital motion.

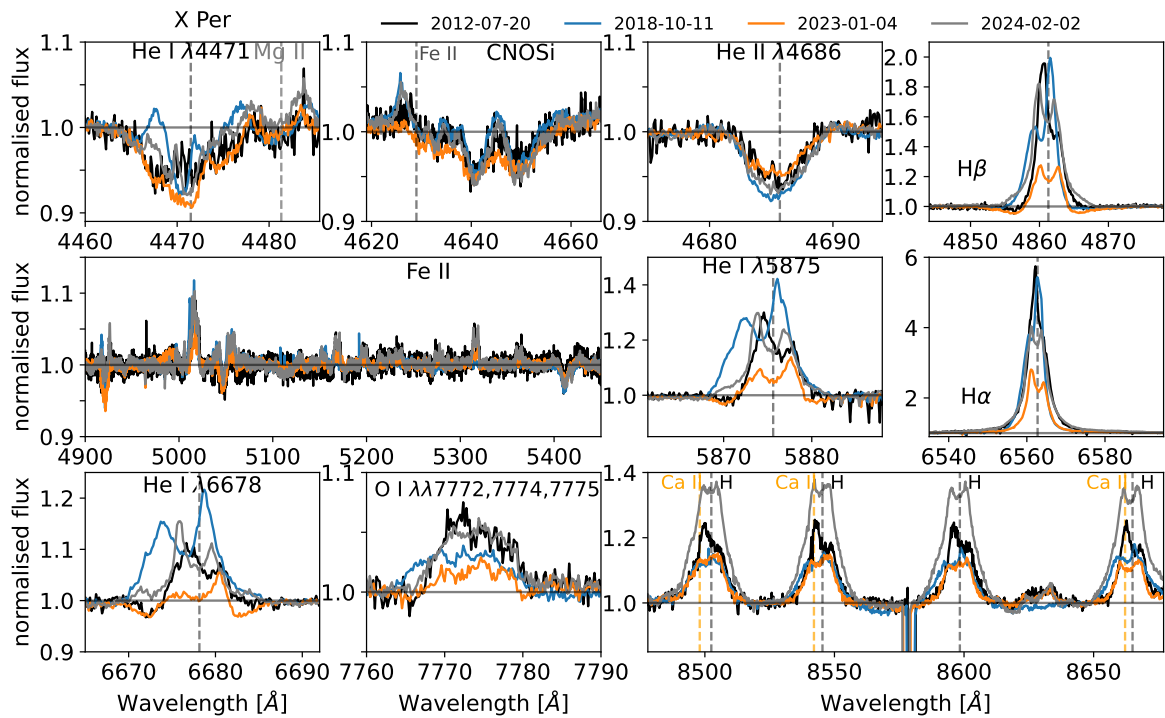


Fig. A7: Spectra for X Per showing strong variability in V/R and line strength.

Table A1: Nature of typical spectral lines for the different targets.

spectral line	EM* VES 826	HD 259440	V420 Aur	V615 Cas	V725 Tau	V831 Cas	X Per
H α	dp	e	a	dp	e/dp	dp	e/dp
H β	dp	a + dp	dp	dp	dp	dp/Pc	dp
H γ	a + dp	a + dp	a + dp	a + e	a + dp	a + P _c	a + dp
H Paschen (λ 8000-9000)	dp	dp + Ca	dp + Ca	a/dp	dp	a	e
He I λ 4009	/	a	a	a	a	a	a
He I λ 4026	a (weak)	a	a	a	a	a	a
He I λ 4121	a	a	a	a	a	a	a
He I λ 4144	a (weak)	a	a	a	a	a	a
He I λ 4388	a	a + e	a + e	a	a	a	a
He I λ 4471	a	a	a	a	a + e	a	a + e
He I λ 4713	a	a (weak)	a	a	a	a + e	dp?
He I λ 4922	a + Fe?	a + Fe	a + e + Fe	a	a + Fe	a + e	a + e
He I λ 5016	e	a + Fe	e + Fe	a	dp	dp	dp + Fe
He I λ 5048	a	a	a	a + Fe?	a + Fe?	a	a + e
He I λ 5876	dp	a + dp	dp	dp	dp	dp/Pc	dp
He I λ 6678	dp	a + dp	a + e	dp	dp	Pc	dp
He II λ 4686	a	/	a (weak)	/	a	/	a
He II λ 5412	a	/	/	a	a	/	a
O I $\lambda\lambda$ 7772,7774,7775	e (weak)	e	e	a	e	a	e
C-N-O-Si $\lambda\lambda$ 4630-4655*	a	a + Fe	a + Fe	a	a	a	a + e?
Fe II emission lines	/	dp	dp	e (weak)	/	/	e

Notes. Explanation of the abbreviations: a = absorption, dp = double-peaked, e = emission non-dp, Fe = Fe II emission, Ca = Ca II emission, P_c = P-cygni like profile. A lone dash indicates absence of the line or a non-detection. A dash in between abbreviations means a changing profile. * Includes the following lines: N II $\lambda\lambda$ 4631,4643, Si IV $\lambda\lambda$ 4631,4654, N III $\lambda\lambda$ 4634,4641, O II $\lambda\lambda$ 4639,4642,4649,4651, and C III $\lambda\lambda$ 4647,4650,4651.

Appendix B: The choice of the boundaries for the bisector method

For the bisector method, we exclude the bottom and top part of the spectral lines. Here, we investigate how the measured RVs depend on the chosen fraction of the line to exclude by varying

the percentage of the line that is excluded from the bottom and the top. A part of the top is preferentially excluded because of the large variability that is sometimes seen in the top regions of the emission lines due to variability in the disc.

Fig. B1 shows RVs measured for V420 Aur using different cuts on H α . The top panel shows the absolute RVs. While the sys-

temic velocities differ between different cuts, the different sets of RVs follow the same general trend. This can be more clearly

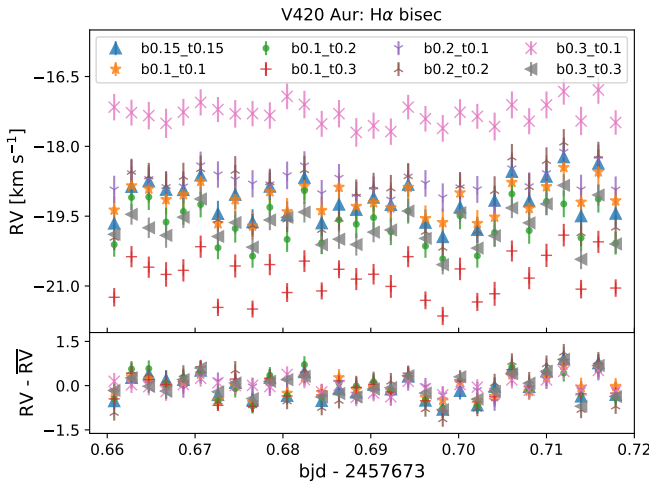


Fig. B1: Radial velocities for V420 Aur obtained with the bisector method using different cuts on the $H\alpha$ emission line. Top panel shows absolute RVs. Bottom panel shows the mean-subtracted RVs. In the legend, the fractions that are excluded starting from the bottom and top of the line come after the letter ‘b’ and ‘t’, respectively.

seen in the mean-subtracted RVs, which are shown in the bottom panel of Fig. B1.

The systemic velocities between different cuts are slightly offset from one another, with the largest offsets observed when excluding a larger fraction starting from the top (red pluses) or the bottom (pink crosses). The different systemic velocities indicate that the upper part of the line profile of $H\alpha$ for V420 Aur is more redshifted and the bottom part more blueshifted. Something similar is also seen when repeating this for $H\beta$. While this reveals how the line is shaped, it is beyond the scope of this work to research in detail the shape of the line profiles.

In this work, we are not aiming to determine the systemic velocities of the BeXRBs but determine whether we can see orbital motion. Since the different cuts follow the same general trend, we will further use only one cut. We will choose to exclude 10% of the bottom and top (orange stars in Fig. B1).

Appendix C: Radial-velocity precision

Table C1 lists the average RV measurement uncertainty $\bar{\sigma}$ and rms values for different spectral lines and methods for a short (V420 Aur: night of 16 October 2016; HD 259440 and V615 Cas: average value of nights with three consecutive measurements) data set ($\text{rms}_{\text{short}}$). The results are illustrated in Fig. 2.

Table C1: Values for $\bar{\sigma}$ and $\text{rms}_{\text{short}}$.

Method	spectral line	V420 Aur		HD 259440		V615 Cas	
		$\bar{\sigma}$ [km s ⁻¹]	$\text{rms}_{\text{short}}$ [km s ⁻¹]	$\bar{\sigma}$ [km s ⁻¹]	$\text{rms}_{\text{short}}$ [km s ⁻¹]	$\bar{\sigma}$ [km s ⁻¹]	$\text{rms}_{\text{short}}$ [km s ⁻¹]
CC	$H\alpha$	0.30	0.25	0.17	0.12	0.48	0.34
	$H\alpha$ cut	0.38	0.72	0.19	0.05	0.77	0.48
	$H\alpha$ abs	-	-	-	-	1.51	0.28
	$H\beta$	0.50	0.71	0.33	0.44	1.07	1.29
	$H\beta$ cut	1.25	2.27	0.63	0.47	-	-
	$H\beta$ abs	-	-	-	-	1.23	1.13
	$H\gamma$	-	-	0.71	0.85	2.08	6.25
	H pas	0.66	1.13	0.40	0.49	-	-
	Fe	0.88	1.66	0.55	1.00	-	-
	He I abs	1.63	3.28	3.63	9.11	1.70	6.46
	He I em	-	-	0.83	1.34	0.70	2.07
	O I 7774	2.46	4.39	1.29	1.94	-	-
	He II	-	-	-	-	4.69	16.05
	He I + II abs	-	-	-	-	1.61	7.19
	He I + II + O I	-	-	-	-	1.58	6.26
lpf	CNOSi	2.22	3.85	2.99	6.77	8.11	39.78
	Ca II triplet	-	-	0.34	0.19	-	-
bise	$H\alpha$	0.23	0.25	0.23	0.14	2.71	3.90
	$H\alpha$ double	-	-	-	-	0.62	1.11
	$H\alpha$ cut	0.17	0.22	-	-	0.80	0.65
	$H\beta$	1.13	1.35	0.32	0.42	2.08*	1.22*
	$H\beta$ double	0.46	0.78	0.97	4.16	1.21	2.90
	$H\beta$ cut	0.52	0.97	-	-	3.51	6.90
	$H\gamma$	-	-	-	-	8.69*	4.20*
bise	$H\alpha$	0.24	0.34	0.15	0.16	0.41	1.54
	$H\beta$	0.23	1.43	0.08	0.51	0.27	8.03

* Gaussian fit was an absorption line.

Appendix D: Periodograms

Here, we present in detail the periodograms of the targets, which were calculated using the metric introduced in Saha & Vivas (2017). Instead of using the generalised Lomb-Scargle (gLS) Fourier-transform method (Lomb 1976; Scargle 1982), Saha & Vivas (2017) made use of phase-dispersion minimisation (PDM; Stellingwerf 1978), which is based on the principle that, for the true period, the scatter of the data in different phase bins must be minimal. Moreover, the size of the bins can be varied for different trial periods for sparse data. Saha & Vivas (2017) showed that the adapted periodogram metric 2gLS/PDM, which was used in this work, is more reliable for sparsely distributed data. Periodograms are shown in Fig. D1.

For none of the seven BeXRBs is the X-ray orbital period the most significant period in the periodograms. This thus already indicates difficulties in finding independent orbital solutions. Hence, for most targets, the information of the X-ray orbital period is crucial to find orbital solutions.

One of the main reasons for this is most likely the combination of the sparse sampling of the data for many of the targets and the large spectral changes over the time course of years. Indeed, for EM* VES 826 and HD 259440 there is a local maximum around the reported X-ray period, which could become more significant with more data.

V725 Tau and X Per are two examples of systems that exhibit large-scale variability (see Figs. A5 and A7). For neither is the X-ray orbital period retrieved. Instead, the periodograms of emission lines suggest a much longer period, likely due to the large blue-shift in the RVs induced by the spectral changes. Even with the absorption lines, the X-ray orbital period is not recovered. Instead, the highest-amplitude period for He I abs is longer, but closer to the X-ray orbital period.

For V615 Cas, He I abs show a clear period close to the previously reported period of 26.5 d. For the emission lines, the highest-amplitude period is \sim 31 d. Due to the large density of peaks present in the periodograms of V615 Cas, the X-ray orbital period is not the highest-amplitude period. The 31 d period might be a beat period due to a precessing disc.

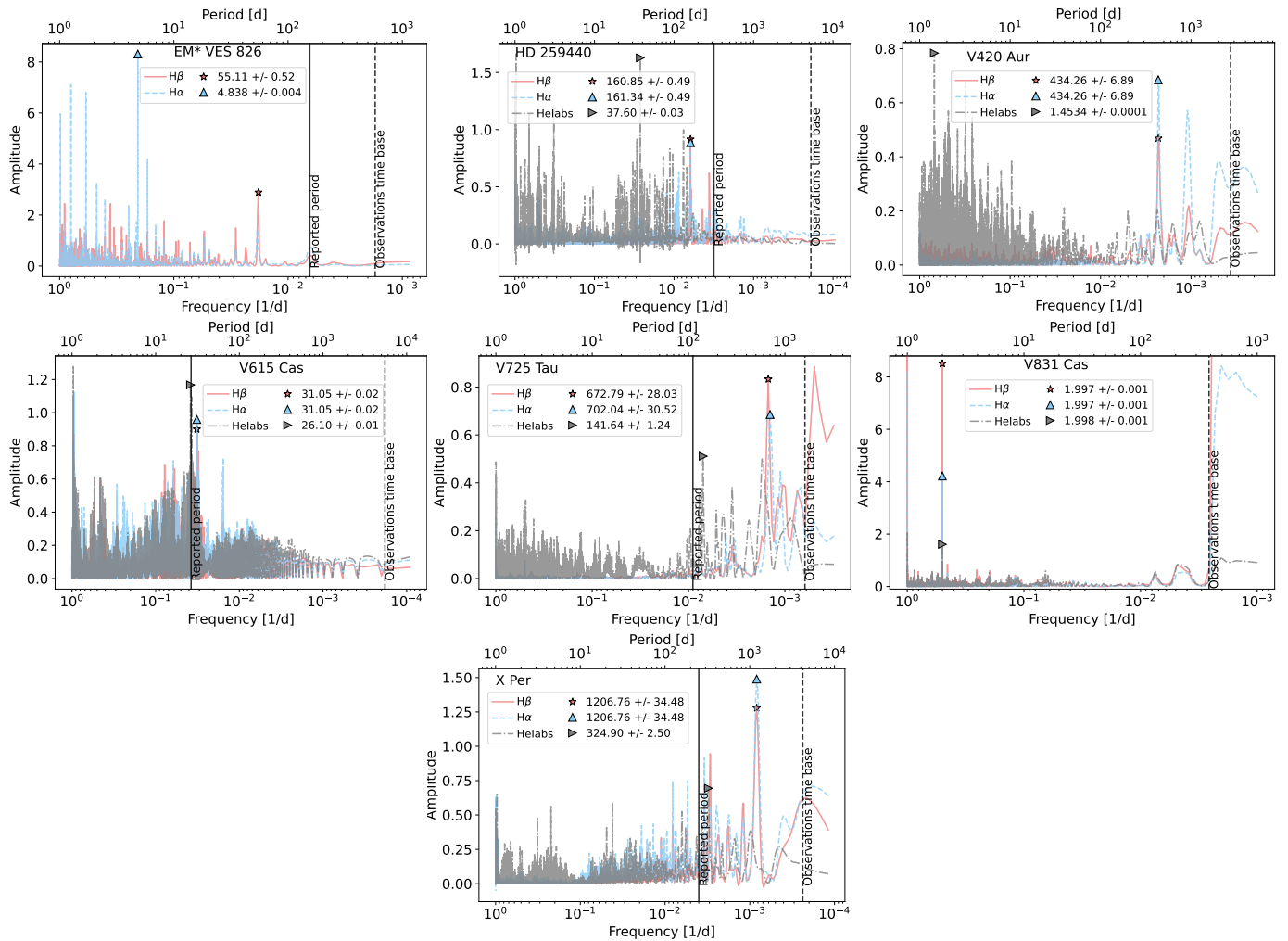


Fig. D1: Periodograms for $H\beta$, $H\alpha$, and He I abs (if available). Highest-amplitude frequencies are marked with a black-edged symbol with their value listed in the legends in units of days. Vertical solid-black and dashed-black lines indicate the reported X-ray orbital period and the observation time span, respectively. Each panel shows a different system.